ICEE
Intelligent Computing for Energy and Environment
ISSN 2979-6717

Review Article | Intelligent Computing for Energy and Environment | Vol. 1, No. 1 (2026) | DOI: https://doi.org/10.68992/icee.2026.2090

Fundamental Physics and Constitutive Modeling for Underground Hydrogen Storage

Transport Phenomena, Displacement Mechanisms, and Trapping

Mohamed Fathy El-Amin *[1,2]

[1]*Energy Research Laboratory, College of Engineering, Effat University, Jeddah 21478, Saudi Arabia*
[2]*Mathematics Department, Faculty of Science, Aswan University, Aswan 81528, Egypt*

Corresponding author: *Mohamed F. El-Amin | momousa@effatuniversity.edu.sa | 0000-0003-2513-6791*

Received 20 July 2026 **Accepted** 12 Aug 2026 **Published** 13 Aug 2026
Handling Editor Jisheng Kou; Badre Bossoufi

ABSTRACT

Underground hydrogen storage (UHS) in porous geological formations requires an understanding of hydrogen-specific transport physics that differs fundamentally from natural gas and CO_2 systems. This review, the first of a two-part series, synthesizes the subsurface physics controlling hydrogen migration, displacement, trapping, and diffusive transport. Hydrogen's extreme mobility contrasts with formation brine, promoting viscous fingering and reducing sweep efficiency during injection and production operations. We present fractional flow analysis, dimensionless scaling using capillary, gravity, Bond, and Peclet numbers, and stability criteria for characterizing displacement fronts. Trapping mechanisms—structural, residual, solubility, and mineral—are quantified using hydrogen-specific parameterizations, including Land-type models for residual-trapping hysteresis. Diffusive transport is assessed across regimes ranging from continuum Fickian behavior in reservoir rocks to slip and Knudsen diffusion in tight caprocks, using Knudsen-number criteria for regime selection. Thermal effects, particularly Joule–Thomson cooling during expansion, are reviewed for their impact on near-wellbore processes. This review provides practitioners with the physical framework and parameter ranges needed to select appropriate models for reservoir simulation, with emphasis on the quantitative differences between hydrogen and other stored gases. Next work addresses constitutive modeling, geochemical/microbial interactions, and field-scale considerations.

Keywords: *underground hydrogen storage; multiphase flow; hydrogen trapping; diffusion; capillary pressure; mobility ratio; viscous fingering; Knudsen diffusion*

1 Introduction

The global transition toward sustainable energy systems has positioned hydrogen as a critical energy carrier for decarbonization, with underground geological formations emerging as the most viable option for large-scale, long-term storage [1]. Unlike batteries or above-ground tanks, geological storage in depleted hydrocarbon reservoirs, saline aquifers, and salt caverns offers capacities measured in terawatt-hours—sufficient to buffer seasonal variations in renewable energy production and provide strategic reserves [2, 3].

Hydrogen's unique molecular properties introduce physical phenomena that cannot be adequately captured by adapting existing natural gas or CO_2 storage models. Its kinetic diameter of approximately 0.289 nm, the smallest of any gas molecule, enables penetration of pore spaces inaccessible to larger molecules [5]. Its viscosity at reservoir conditions ($\mu_{H_2} \approx 9$ μPa·s) is roughly half that of methane and one-third that of CO_2, creating highly unfavorable mobility ratios that promote viscous fingering and reduce sweep efficiency

[6]. These characteristics necessitate rigorous understanding of the underlying physics specific to hydrogen systems.

This review is the first of a two-part series that provides comprehensive coverage of the physics and modeling of underground hydrogen storage (UHS). This paper focuses on the fundamental transport phenomena: multiphase flow and displacement, trapping mechanisms, diffusive processes, and thermal effects.

1.1 Scope and Objectives

The fundamental conservation equations governing multiphase flow in porous media—mass, momentum, and energy balances—are grounded in first-principles physics and apply universally regardless of the fluid system. Darcy's law, capillary pressure–saturation relationships, and Fickian diffusion describe transport for any fluid. The critical distinction lies not in the governing equations but in the *constitutive parameters* that close them: relative permeability curves, capillary pressure functions, diffusion coefficients, interfacial tensions, and contact angles.

The objectives of of this review are to:

- Synthesize the physical mechanisms controlling hydrogen migration and displacement in porous media
- Quantify hydrogen-specific mobility contrasts and their implications for displacement stability
- Present dimensionless scaling frameworks for regime classification
- Review trapping mechanisms with hydrogen-specific parameterizations
- Assess diffusive transport across relevant regimes from reservoir to caprock
- Identify where hydrogen behavior diverges quantitatively from CH_4 and CO_2 analogues

1.2 Organization

Section 2 reviews geological formations suitable for UHS and their characteristic properties. Section 3 presents multiphase flow physics, including fractional flow analysis, mobility ratios, dimensionless scaling, and viscous fingering criteria. Section 4 addresses trapping mechanisms. Section 5 covers diffusion and dissolution processes. Section 6 examines thermal effects. Section 7 provides conclusions and identifies research gaps addressed further in future review work.

2 Geological Formations and Storage Characteristics

The choice of geological formation fundamentally determines which physical processes dominate hydrogen behavior and consequently which constitutive models are required for accurate simulation [1, 2]. Three primary formation types are considered for UHS: salt caverns, depleted hydrocarbon reservoirs, and deep saline aquifers (Figure 1), each presents distinct advantages, challenges, and modeling requirements.

2.1 Salt Caverns

Salt caverns created by solution mining in bedded or domal salt formations offer several advantages for hydrogen storage: exceptionally high injection and production rates (enabling response to rapid demand fluctuations), minimal hydrogen losses due to the virtual impermeability of salt ($k < 10^{-21}$ m^2), and proven long-term integrity from decades of natural gas storage experience [3, 18].

The physics of salt cavern storage differs fundamentally from porous media storage. In the absence of a porous matrix, flow within the cavern is governed by single-phase gas dynamics rather than multiphase Darcy flow. The primary physical challenges involve thermodynamic behavior of the stored gas (compression/expansion during cycling), heat transfer with the surrounding salt, and geomechanical stability under cyclic pressure and thermal loading [16, 17].

Salt exhibits time-dependent creep deformation described by Norton power-law or more sophisticated multi-mechanism models [16]. Under the deviatoric stresses induced by cavern pressure cycling, the salt slowly deforms, potentially leading to volume loss and eventual convergence. This geomechanical complexity,

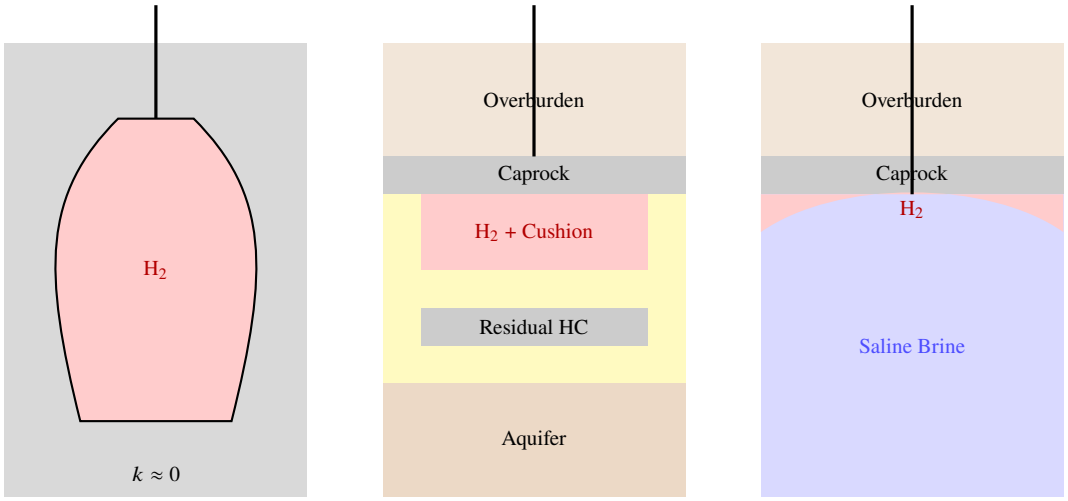


Figure 1. Schematic comparison of the three primary geological formation types for underground hydrogen storage.

rather than multiphase flow, dominates modeling requirements for salt cavern storage and is addressed in detail in the companion review on salt cavern geomechanics.

Operational experience from facilities including Teesside (UK), Clemens Dome (USA), and Moss Bluff (USA) demonstrates that salt caverns can reliably store hydrogen over decades with minimal losses [18]. The Teesside facility operated from 1972 to 2016, storing hydrogen for industrial applications with documented losses below detection limits.

2.2 Depleted Oil and Gas Reservoirs

Depleted hydrocarbon reservoirs represent attractive UHS targets due to the availability of existing infrastructure (wells, surface facilities, pipelines), extensive geological characterization from production history, and proven seal integrity demonstrated by hydrocarbon retention over geological timescales [10, 71]. However, the presence of residual fluids and established microbial communities introduces several physical processes requiring careful modeling consideration.

2.2.1 Compositional Mixing

Injected hydrogen inevitably mixes with residual hydrocarbons (primarily methane in gas reservoirs, heavier components in oil reservoirs) and any deliberately introduced cushion gas [19, 21]. The extent and rate of mixing depend on multiple factors:

Density contrasts: Hydrogen density under typical subsurface conditions is on the order of ~ 8–16 kg/m^3 (e.g., ~ 7.7 kg/m^3 at 10 MPa, 25°C; ~ 16.4 kg/m^3 at 25 MPa, 323 K), which is far lower than methane at comparable conditions (e.g., ~ 125–138 kg/m^3 at 20 MPa and 320–340 K). These contrasts promote buoyancy-driven segregation, with hydrogen tending to migrate upward and accumulate beneath the caprock and toward structural highs, which can enhance hydrogen enrichment in upper parts of the storage structure [22].

Dispersion: Mechanical dispersion during flow through heterogeneous porous media spreads the mixing zone between hydrogen and other gases. Longitudinal dispersivities typically range from 0.1–10 m depending on formation heterogeneity, while transverse dispersivities are typically 10–100 times smaller [21].

Molecular diffusion: Even in the absence of advective flow, molecular diffusion gradually homogenizes gas composition. For dilute gases, D is approximately inversely proportional to pressure ($D \propto 1/p$) and increases with temperature [36]. For the H_2–CH_4 pair, recommended correlations give $D_{H_2-CH_4} \approx (6.7\text{–}7.0) \times 10^{-5}$ m^2/s at ~298 K and ~1 bar, implying faster compositional mixing than in typical natural-gas systems [37].

Cycling frequency: UHS is a cyclical operation that may serve daily, weekly, or seasonal load leveling, depending on market requirements; however, depleted gas reservoirs are generally expected to operate seasonally with one or two cycles per year [23]. Cycling duration and the number of cycles can affect the purity of the extracted hydrogen: purity is expected to improve as the number of cycles increases, and longer time periods between cycles allow gravitational separation between hydrogen and in-situ fluids [23]. The extracted gas stream may require treatment to meet the required hydrogen specifications [23]. Seasonal field-scale simulations also show that using formation gas as cushion gas can increase ultimate hydrogen recovery but at the cost of hydrogen purity, and injecting an H_2–formation-gas mixture can lead to a varying hydrogen fraction in the withdrawn gas [13]. Gas mixing is governed by molecular diffusion and mechanical dispersion (velocity-dependent), and compositional simulation is used to predict the produced-gas composition during cyclic operation [21]. Withdrawal purity also depends strongly on hydrodynamics and the evolution of the H_2–cushion-gas mixing zone (e.g., CO_2 solubility effects in gravity-stable vs viscous-dominated regimes) [22]. Compositional modeling with an appropriate equation of state is therefore important for forecasting withdrawal composition and purity [23].

2.3 Deep Saline Aquifers

Deep saline aquifers can provide very large storage capacity for seasonal-to-interseasonal energy storage. In particular, porous saline aquifers and depleted hydrocarbon fields offer storage capacities several orders of magnitude larger than salt caverns, but suitable sites require specific characterization to ensure secure and economic injection and reproduction [1].

2.3.1 Hydrogen Dissolution

Hydrogen dissolves into formation brine and can be transported in the aqueous phase. Dissolution can represent both a trapping mechanism and a loss pathway, and solubility depends strongly on pressure, temperature, and salinity [27, 28, 29]. A common representation is Henry's-law-type behavior,

$$x_{H_2} = \frac{f_{H_2}}{H(T)}, \tag{1}$$

where x_{H_2} is the aqueous-phase mole fraction, f_{H_2} is hydrogen fugacity, and $H(T)$ is the temperature-dependent Henry constant.

Depth-based calculations indicate that hydrogen solubility can become appreciable under subsurface conditions. For example, at about 1000 m depth (roughly ~100 bar under hydrostatic conditions), hydrogen solubility in pure water is on the order of 0.07 mol/kg_{H_2O} [28]. Salinity reduces solubility via a salting-out effect; at the investigated depths, solubility is about 35% lower in 1 mol/kg_{H_2O} NaCl brine than in pure water, and about 30% lower in 2 mol/kg_{H_2O} NaCl than in 1 mol/kg_{H_2O} NaCl [28].

For underground storage conditions (typically below about 60°C), pressure is a key factor governing phase equilibrium, while salinity plays a secondary (but non-negligible) role [28]. Accurate solubility modeling in brines may require electrolyte-capable thermodynamic models; for example, Lopez-Lazaro et al. discuss parameterization of the Søreide–Whitson framework for H_2–H_2O–NaCl [28].

2.3.2 Capillary Trapping in Heterogeneous Media

After injection ceases, capillary trapping can immobilize portions of the gas phase as disconnected ganglia, limiting plume migration over long timescales; this mechanism is well established in the context of CO_2 storage and is relevant to gas storage more broadly [30]. The degree and spatial distribution of trapped gas will depend on rock structure, capillary properties, and heterogeneity.

Table 1. Comparison of physical processes and modeling requirements for different geological storage types [1, 2, 3].

Aspect	Salt Caverns	Porous Media (Reservoirs/Aquifers)
Primary physics	Thermodynamics, geomechanics, heat transfer	Multiphase flow, capillarity, transport
Flow equations	Single-phase compressible gas dynamics	Darcy-scale multiphase flow
Key constitutive models	Creep laws (Norton, Munson-Dawson), gas EOS	$k_r(S)$, $p_c(S)$, hysteresis models
Dominant uncertainties	Cavern geometry, creep parameters, thermal properties	Permeability heterogeneity, wettability, microbial kinetics
Cyclic effects	Salt fatigue, thermal stress cycling	Saturation hysteresis, residual trapping evolution
Typical capacity	10^6–10^8 m^3 (STP) per cavern	10^8–10^{10} m^3 (STP) per formation
Cycling rate capability	Hours to days (high deliverability)	Days to months (rate limited by injectivity)
Hydrogen losses	Negligible (impermeable salt)	1–20% (dissolution, diffusion, microbial)
Infrastructure needs	Solution mining, brine disposal	May use existing wells (depleted reservoirs)

2.3.3 Long-Distance Plume Migration

In laterally extensive aquifers, buoyancy provides a characteristic driving force that can promote segregation and, when a lateral pressure/height gradient exists (e.g., sloping caprock or thickness variations), lateral plume migration. A convenient Darcy-scale buoyancy velocity is

$$u_b \sim \frac{k\,\Delta\rho\,g}{\mu_g}, \tag{2}$$

which follows from balancing Darcy flow with hydrostatic pressure gradients and is widely used in porous gravity-current scalings [33].

If one wishes to express an average gas velocity within the gas-filled pore space, the corresponding seepage (pore) velocity scale is obtained by dividing the specific discharge by the available pore fraction,

$$v_b \sim \frac{u_b}{\phi S_g} \sim \frac{k\,\Delta\rho\,g}{\mu_g\,\phi\,S_g}, \tag{3}$$

(using the standard conversion from specific discharge to seepage velocity by division by porosity [34]). In multiphase settings, a relative-permeability factor k_{rg} is commonly included, i.e. $u_b \sim k k_{rg} \Delta\rho g/\mu_g$.

It is noteworthy that this is an order-of-magnitude estimate for the characteristic velocity scale, not a predictive formula.

2.4 Modeling Implications by Formation Type

The foregoing discussion illustrates that different geological settings require fundamentally different modeling approaches. Table 1 summarizes these distinctions to guide model selection.

3 Multiphase Flow Physics

Hydrogen storage in porous media inherently involves at least two fluid phases: a hydrogen-rich gas phase and an aqueous brine phase [6]. In depleted reservoirs, residual hydrocarbons may constitute a third phase. Understanding the physics governing the interaction of these phases, the competition between viscous, capillary, and gravitational forces, is fundamental to predicting storage performance and selecting appropriate constitutive models.

3.1 Hydrogen Fluid Properties

The unique physical properties of hydrogen, relative to other subsurface gases, strongly influence multiphase flow and mass transfer in porous media. Table 2 summarizes representative values and ranges for key parameters controlling mobility, buoyancy, capillarity, dissolution, and diffusion. Because some properties are basis-dependent (gas-phase versus aqueous/brine phase, and temperature/salinity), the table explicitly reports the reference conditions for each entry.

Several features in Table 2 merit emphasis. First, at typical reservoir pressures and temperatures, hydrogen's density is substantially lower than methane and far lower than dense or supercritical CO_2 when present, amplifying buoyancy forces and accelerating vertical segregation and gravity override. Second, hydrogen's viscosity is lower than methane and CO_2, increasing mobility; during gas–gas or gas–brine displacement this can produce unfavorable mobility ratios and promote viscous fingering unless counteracted by capillary forces, gravity stabilization, or operational controls. Third, hydrogen exhibits comparatively high aqueous diffusivity; even when aqueous diffusivities are reported at a different basis temperature (e.g., 25°C in standard compilations), the ordering typically persists and indicates enhanced diffusive mass transfer and more rapid mixing/dissolution when brine contact is significant. Fourth, hydrogen deviates from ideal-gas behavior at elevated pressures, with Z measurably different from unity (often slightly above 1 in the relevant regime), so density and related transport predictions should rely on an appropriate equation of state rather than ideal-gas assumptions.

Table 3 compares the mobility characteristics of hydrogen with other gases commonly encountered in underground storage operations. The substantially higher mobility ratio for H_2 relative to CH_4, CO_2, and N_2 has direct implications for displacement efficiency, fingering tendency, and ultimate recovery.

Table 2. Physical properties of hydrogen compared with methane and CO_2. Gas-phase properties are reported at reservoir conditions (100 bar, 50°C) where indicated; aqueous/brine properties are reported at the basis stated in the last column. Data compiled from [12, 4, 27, 36].

Property	H_2	CH_4	CO_2	Units	Basis (T, P, phase)
Molecular weight	2.02	16.04	44.01	g/mol	intrinsic
Kinetic diameter† [12]	0.289	0.380	0.330	nm	intrinsic (commonly tabulated)
Density	7–12	65–80	200–600[a]	kg/m^3	gas, 100 bar, 50°C
Dynamic viscosity	9–10	13–16	20–50[a]	μPa·s	gas, 100 bar, 50°C
Compressibility factor Z	1.04–1.06	0.85–0.90	0.3–0.7[a]	–	gas, 100 bar, 50°C
Diffusivity in water [36]	4.50	1.49	1.92	$\times 10^{-9}$ m^2/s	water, 25°C, infinite dilution
IFT with brine [4]	50–70	40–60	20–35	mN/m	brine, range across reported P–T–salinity in review
Solubility in brine [27]	0.8–1.2	–	–	mmol/kg/MPa	H_2: brine (H_2O+NaCl), 323–373 K, up to ~23 MPa; CH_4/CO_2: see note[b]
Critical temperature	33.2	190.6	304.2	K	intrinsic
Critical pressure	13.0	46.0	73.8	bar	intrinsic

Table 3. Comparison of mobility characteristics for gases in underground storage. Conditions: 100 bar, 50°C, brine viscosity $\mu_w \approx 0.5$ mPa·s. Mobility ratio $M = \lambda_g/\lambda_w = (k_{rg}/\mu_g)/(k_{rw}/\mu_w)$ evaluated at endpoint saturations.

Property	H_2	CH_4	CO_2	N_2	Units
Fluid properties at 100 bar, 50°C					
Gas viscosity μ_g	9–10	15–18	20–25[a]	20–22	μPa·s
Gas density ρ_g	7–8	65–75	200–700[a]	100–115	kg/m^3
Viscosity ratio μ_w/μ_g	50–55	28–33	20–25	23–25	–
Mobility characteristics					
Typical M (endpoint)[b]	20–100	10–30	2–15[a]	10–25	–
Fingering tendency[c]	Severe	Moderate	Mild–Moderate	Moderate	–
Gravity number N_g[d]	High	Moderate	Low–High[a]	Moderate	–
Displacement efficiency					
Breakthrough S_w^*[e]	0.55–0.70	0.45–0.55	0.35–0.50	0.45–0.55	–
Sweep efficiency[f]	40–60%	55–70%	60–80%	55–70%	–
Recovery factor (1st cycle)	50–80%	70–90%	80–95%	75–90%	–
Operational implications					
Cushion gas fraction	40–60%	30–40%	20–35%	30–40%	–
Cycling stability	Builds slowly	Stable	Stable	Stable	–

The extreme mobility contrast for hydrogen ($M \sim 20$–100 compared to $M \sim 2$–15 for CO_2) explains several operational challenges specific to UHS. First, viscous fingering during injection reduces volumetric sweep efficiency to 40–60%, requiring larger cushion gas volumes (40–60% of working gas) compared to natural gas storage (30–40%). Second, early gas breakthrough during withdrawal leads to lower first-cycle recovery factors (50–80%) that improve gradually as residual saturations stabilize over multiple cycles [1]. Third, the high gravity number partially compensates for unfavorable viscous effects by promoting gravity segregation, which concentrates hydrogen at structural highs and can improve withdrawal purity. These trade-offs between viscous instability and gravity segregation are central to UHS design optimization.

3.2 Hydrogen-Brine Interfacial Properties

Recent experimental and computational studies have substantially expanded the database for H_2–brine interfacial tension under reservoir conditions. Hosseini et al. [72] measured IFT over temperatures of 298–423 K, pressures of 2.8–34.5 MPa, and salinities up to 5 mol/kg using the pendant drop method, finding that IFT decreases linearly with increasing pressure and temperature while increasing with salinity. Chow et al. [73] reported IFT for H_2–H_2O and H_2–CO_2–H_2O systems at pressures up to 45 MPa and temperatures of 298–448 K, providing baseline data for cushion gas scenarios. Mirchi et al. [48] demonstrated that CH_4 addition to the gas phase reduces H_2–brine IFT, with implications for cushion gas selection in depleted gas reservoirs.

Machine learning approaches have been developed to predict IFT across broader parameter ranges than covered by experiments alone. Xie et al. [74] used molecular dynamics to generate 840 data points for (H_2+CO_2)–brine systems and developed ML-based correlations achieving $R^2 = 0.902$ against experimental data. Behnamnia et al. [75] applied hybrid ML techniques to model IFT in H_2–cushion gas–brine systems for geological storage applications. These predictive tools enable IFT estimation under conditions not yet measured experimentally, though validation against new measurements remains essential.

3.3 Fractional Flow

The fractional flow of the wetting phase directly relates to mobility ratio through [31]:

$$f_w = \frac{1}{1 + \frac{k_{rg}}{k_{rw}} \cdot \frac{1}{M_\mu}}, \tag{4}$$

where $M_\mu = \mu_w/\mu_g$ is the viscosity ratio. For hydrogen ($M_\mu \approx 50$–100), the adverse mobility produces a fractional flow curve that rises steeply at low water saturations compared to CH_4 ($M_\mu \approx 15$–30) and CO_2 ($M_\mu \approx 5$–15) [32].

The Buckley-Leverett theory describes saturation front propagation, with shock-front saturation S_w^* determined by the Welge tangent construction [31]. For hydrogen, the steep fractional flow curve yields $S_w^* \approx 0.3$–0.4, compared to $S_w^* \approx 0.5$–0.6 for CO_2 [6]. This results in earlier water breakthrough and extended two-phase production periods.

The adverse fractional flow behavior reduces displacement efficiency at breakthrough by 20–30% compared to methane. Combined with hysteretic trapping during withdrawal, this contributes to working gas recovery factors of 50–80% for UHS versus >90% for natural gas storage [1, 9]. Lower displacement efficiency also necessitates larger cushion gas volumes.

Gravity modifies the fractional flow through the density contrast ($\Delta\rho \approx 990$–1050 kg/m^3 for H_2-brine), which can stabilize or destabilize displacement depending on flow orientation. Capillary effects introduce dispersion of the shock front, reducing fingering intensity but increasing mixing zone thickness during cyclic operations.

3.4 Mobility Ratio and Displacement Stability

For immiscible displacement, the mobility ratio is commonly used as a first-order indicator of viscous stability [41]:

$$M = \frac{\lambda_{\text{displacing}}}{\lambda_{\text{displaced}}} = \frac{k_{r,g}/\mu_g}{k_{r,w}/\mu_w}, \tag{5}$$

where $\lambda_\alpha = k\, k_{r,\alpha}/\mu_\alpha$ is the phase mobility and subscripts g and w denote gas and water/brine. In practice, M should be evaluated consistently at the relevant saturation state (e.g., near the displacement front or using endpoint values as an approximation).

For hydrogen displacing brine during injection, the viscosity contrast is large (order $\mu_w/\mu_{H_2} \sim 50$–100 depending on temperature and salinity), and endpoint relative permeabilities vary widely across rocks and measurement protocols. Using representative endpoint ranges (e.g., $k^0_{r,g} \sim 0.5$–0.8 and $k^0_{r,w} \sim 0.3$–0.5 as an illustrative approximation), mobility ratios are typically unfavorable, yielding $M \sim O(10)$–$O(10^2)$. Such $M > 1$ conditions increase the propensity for viscous fingering, although the onset and severity also depend on capillarity, dispersion, gravity, and heterogeneity [41].

The practical consequences of unfavorable mobility (and the associated tendency toward unstable displacement) include reduced sweep efficiency and channeling, which can lead to earlier gas production and non-uniform plume development. In the context of underground hydrogen storage, an additional and widely noted consequence is increased mixing/contamination with residual or cushion gas, which can reduce withdrawal purity and effective recoverability; numerical studies summarized by Okoroafor et al. show that hydrogen may infiltrate the cushion gas near injectors, hindering piston-like displacement and degrading recovery performance in viscous-dominated regimes [9, 41]. The quantitative impact of these mobility effects on displacement and recovery efficiency is formalized through fractional flow analysis in the following subsection.

Mobility contrast and phase-segregation regime

For an injection scenario in which buoyancy acts perpendicular to the mean flow direction, the relative importance of viscous and gravity forces determines whether the displacement is gravity-stable, mixed, or gravity-overridden. A convenient scaling compares the characteristic time for vertical buoyancy segregation, $t_b \sim H\,\phi\,\mu_g/(k\,k_{r,g}\,\Delta\rho\,g)$, with the characteristic time for horizontal viscous advection across the swept zone, $t_v \sim L\,\phi/u$, where H and L are the vertical and lateral extents of the swept region and u is the Darcy velocity. The ratio $t_v/t_b = (L\,\mu_g)/(H\,u) \times (k\,k_{r,g}\,\Delta\rho\,g)/(\mu_g\,u) \sim (L/H)\,N_g$ shows that gravity segregation dominates when the gravity number is large *and* the lateral-to-vertical aspect ratio is high. For H_2–brine with $\Delta\rho \sim 10^3$ kg/m^3, typical UHS scenarios yield $N_g \sim 10$–100 (Table 4), so plumes with even modest aspect ratios ($L/H \gtrsim 1$) tend toward gravity-overridden configurations during slow injection. At elevated injection rates that depress N_g below order unity, viscous forces drive lateral fingering and the M-dominated unstable regime takes over. The transition between these regimes is therefore an operational lever: rate management directly controls which dimensionless number (M or N_g) dominates the segregation pattern, and consequently which constitutive uncertainties (mobility-ratio extrapolations vs. relative-permeability hysteresis) most influence forecast accuracy.

3.5 Capillary Number and Flow Regimes

In addition to the mobility (or viscosity) contrast, the capillary number quantifies the competition between viscous and capillary forces during gas–brine displacement. Following the classical Lenormand-type scaling, the capillary number is defined using the viscosity of the invading (displacing) fluid [38]:

$$Ca = \frac{\mu_i\,u}{\gamma}, \tag{6}$$

where u is a characteristic Darcy velocity, γ is the gas–brine interfacial tension, and μ_i is the viscosity of the invading phase (for H_2 injection in drainage, $\mu_i = \mu_g$).

The pore-scale displacement morphology is commonly interpreted on a (Ca, M) phase diagram, in which the outcome depends on both capillary number and viscosity (or mobility) ratio [38]. At low Ca, capillary forces dominate and the invasion proceeds by capillary-controlled pore-entry events, producing invasion-percolation/capillary-fingering type patterns. As Ca increases, viscous forces become increasingly important; for unfavorable viscosity contrast the displacement tends toward viscous fingering, while for favorable contrast the front can become more stable and compact.

Microfluidic experiments by Lysyy et al. [39] illustrate the strong sensitivity of post-drainage (after injection) gas saturation to Ca in hydrogen–water systems: the reported field-of-view hydrogen saturation after drainage increased from $S_g \approx 0.18$ at $Ca = 7.68 \times 10^{-7}$ to $S_g \approx 0.79$ at $Ca = 3.84 \times 10^{-4}$, consistent with increased viscous influence at higher injection rates.

3.6 Viscous Fingering Analysis

The tendency for viscous fingering during hydrogen injection in brine-saturated porous media is commonly interpreted through mobility contrast and interfacial stability arguments [41]. When the displacing gas exhibits higher mobility than the displaced brine ($M > 1$), perturbations at the front may grow, producing unstable displacement patterns.

Recent pore-scale simulations using micromodels confirm that the observed fingering morphology is not controlled by mobility ratio alone, but strongly depends on injection velocity (or capillary number) and pore geometry [40]. In particular, increasing injection velocity promotes a transition from stable or capillary-controlled invasion toward more viscous-dominated, elongated fingers, while variations in porous structure and porosity significantly reshape finger growth, branching, and sweep. These results emphasize that viscous fingering in UHS is a coupled outcome of viscosity contrast, capillary stabilization, and pore-scale heterogeneity [22, 41, 40].

3.7 Mitigation Strategies for Unstable Displacement

Several operational and engineering strategies can reduce the impact of unstable or highly non-uniform displacement in porous-media UHS. The effectiveness of any strategy is site- and operation-dependent and reflects the interplay of viscous, capillary, gravity, and heterogeneity effects [1, 9].

Injection rate management: Reducing injection rate lowers viscous forcing (and the associated capillary number), thereby decreasing the tendency toward viscous-dominated, unstable displacement. UHS simulations summarized by Okoroafor et al. indicate that at small injection rates gravitational forces can dominate and enable more uniform water displacement, whereas at higher injection rates viscous forces become dominant and displacement becomes unstable with lateral gas fingers [9, 38].

Well placement and completion strategy: Strategic well placement and completion can improve sweep and recovery by controlling plume migration pathways and limiting strong local pressure gradients. For example, UHS studies summarized by Okoroafor et al. show sensitivity to injector placement in dipping structures and improved recovery for extraction wells completed just below the caprock (and wells that do not extend over the full reservoir thickness) [9]. Horizontal wells may further distribute injection/production over longer intervals (thereby lowering local fluxes), but their benefit should be evaluated case-by-case.

Gravity stabilization: In thick or steeply dipping reservoirs, injecting hydrogen at structural highs and displacing brine downward can promote gravity-stable configurations (light gas over dense brine). In the San Pedro dome case study, no viscous fingering was observed despite strong density/viscosity contrast, highlighting the stabilizing role of structural dip and gravity segregation [35].

Cyclic (seasonal) operation: UHS is inherently cyclic (injection/withdrawal over seasons). Studies summarized by Okoroafor et al. indicate that storage-cycle behavior can influence withdrawal performance and mixing outcomes [9]. Any additional benefit from shut-in periods (e.g., redistribution by gravity and capillarity) should be treated as system-specific rather than universal.

Cushion gas selection: Cushion gas choice strongly influences recovery and withdrawal purity. Okoroafor et al. summarize simulation studies comparing methane, nitrogen, and CO_2 cushion gases, reporting that performance metrics (recovery and purity) vary by cushion gas and reservoir scenario [9]. For CO_2 cushion gas specifically, numerical modeling indicates that CO_2 solubility in brine can act as a compositional "filter" that modifies produced-gas purity [22].

3.8 Gravity Effects and Segregation

The large density contrast between hydrogen and brine ($\Delta\rho \approx 990$–1000 kg/m^3) creates strong buoyancy forces driving vertical segregation [35]. The ratio of gravity to viscous forces is characterized by the gravity number:

$$N_g = \frac{k\,\Delta\rho\,g}{\mu_g\,v} \tag{7}$$

For typical UHS parameters ($k \sim 10^{-13}$ m^2, $\Delta\rho \sim 1000$ kg/m^3, $\mu_g \sim 10^{-5}$ Pa·s, $v \sim 10^{-5}$ m/s), $N_g \sim 10$–100, indicating that gravity forces significantly exceed viscous forces and vertical segregation is rapid [35].

The phrase "rapid" merits a quantitative statement. The characteristic buoyancy migration timescale follows from balancing Darcy flow against the hydrostatic pressure gradient: $t_b \sim H\,\mu_g/(k\,k_{r,g}\,\Delta\rho\,g)$, where H is the vertical extent of the plume. Setting $\mu_g = 9 \times 10^{-6}$ Pa·s, $\Delta\rho = 10^3$ kg/m^3, $k_{r,g} = 0.5$, the timescale varies by orders of magnitude across realistic UHS conditions. For $H = 10$ m and $k = 10$ mD, $t_b \approx 20$ days; for $H = 50$ m, $k = 10$ mD, $t_b \approx 100$ days; for $H = 50$ m, $k = 100$ mD, $t_b \approx 10$ days; for $H = 100$ m, $k = 1$ mD, $t_b \approx 2000$ days (5.5 years).

This range spans the operational cycle durations relevant to UHS. For seasonal storage with shut-in periods of 3–6 months, plumes in high-permeability formations ($k \gtrsim 50$ mD) substantially re-equilibrate gravitationally between cycles, while plumes in tight formations ($k \lesssim 1$ mD) do not. The modeling consequence is direct: simulators applying vertical-equilibrium (gravity-segregated) initial conditions to each new injection cycle are

appropriate only when $t_b \ll t_{cycle}$; for tighter formations where this is violated, the residual non-equilibrium state from the previous cycle must be tracked as initial condition. This distinction also affects withdrawal-purity predictions, because incomplete gravity segregation leaves more H_2 co-located with brine, increasing dissolved-phase carry-over during production.

3.9 Peclet Number and Advection-Diffusion Balance

The Peclet number quantifies the relative importance of advective transport to molecular diffusion:

$$\mathrm{Pe} = \frac{v\,L}{D} \tag{8}$$

where v is the characteristic pore velocity, L is a characteristic length scale (typically grain diameter or plume dimension), and D is the molecular diffusion coefficient. For hydrogen in UHS operations, two Peclet number regimes are relevant. Near injection and production wells where velocities are high ($v \sim 10^{-4}$–10^{-3} m/s), Pe $\gg 1$ and advection dominates transport; mixing is controlled by mechanical dispersion rather than molecular diffusion. In the far-field storage zone where velocities decay ($v \sim 10^{-7}$–10^{-6} m/s), Pe approaches unity or below, and molecular diffusion becomes significant for compositional evolution and dissolution into brine. For hydrogen with its high aqueous diffusivity ($D_{H_2} \approx 5 \times 10^{-9}$ m^2/s), the transition to diffusion-dominated behavior occurs at larger length scales than for heavier gases, implying that diffusive losses and mixing may be more significant in quiescent storage zones.

3.10 Bond Number and Gravity-Capillary Balance

The Bond number (or Eötvös number) characterizes the balance between gravitational and capillary forces at the pore scale [38]:

$$\mathrm{Bo} = \frac{\Delta\rho\, g\, L^2}{\gamma} \tag{9}$$

where $\Delta\rho$ is the density difference between phases, g is gravitational acceleration, L is a characteristic pore or grain size, and γ is interfacial tension. For hydrogen–brine systems with $\Delta\rho \approx 1000$ kg/m^3, $\gamma \approx 60$ mN/m, and typical sandstone grain sizes ($L \sim 100$–500 μm), Bo $\sim 10^{-4}$–10^{-3}, indicating that capillary forces dominate at the pore scale. However, at the continuum scale with characteristic lengths of meters to tens of meters, gravitational segregation becomes the controlling factor. This scale-dependent transition explains why pore-scale experiments may not capture the gravity override behavior observed at field scale, and why both capillary trapping (pore scale) and buoyancy-driven migration (field scale) are simultaneously important for UHS. Table 4 summarizes the key dimensionless numbers governing UHS transport phenomena along with their typical ranges for hydrogen systems.

3.10.1 Mechanistic interaction of buoyancy and capillary entry pressure.

The competition between buoyancy and capillary forces determines whether hydrogen can breach the caprock seal. At the gas–water contact, the buoyancy pressure exerted by a hydrogen column of height h is $\Delta p_{buoy} = (\rho_w - \rho_g)gh$. This upward-directed pressure must overcome the capillary entry pressure p_e of the seal before gas can invade. The critical column height at which breakthrough becomes possible is therefore:

$$h_{crit} = \frac{p_e}{(\rho_w - \rho_g)g} = \frac{2\gamma\cos\theta}{r_{throat}(\rho_w - \rho_g)g} \tag{10}$$

For hydrogen with $\gamma \approx 60$ mN/m, $\theta \approx 30$, and $\Delta\rho \approx 1000$ kg/m^3, a shale caprock with $r_{throat} \approx 10$ nm yields $p_e \approx 10$ MPa and $h_{crit} \approx 1000$ m—far exceeding typical storage column heights. However, if the caprock contains larger pore throats (e.g., $r_{throat} \approx 1$ μm in siltstones), p_e drops to ~0.1 MPa and $h_{crit} \approx 10$ m, potentially allowing breakthrough in shallow or thick gas columns. This analysis reveals that seal integrity depends critically on the largest connected pore throats (not mean pore size), and that hydrogen's lower IFT compared to CO_2 reduces h_{crit} by approximately 20–40% for equivalent pore structures.

Table 4. Dimensionless numbers governing UHS transport phenomena: typical H_2 ranges, threshold values, and the modeling decision triggered when the threshold is crossed.

Number	Definition	Physical Meaning	H_2 Range	Threshold and Modeling Decision
Mobility ratio M	$\frac{k_{r,g}/\mu_g}{k_{r,w}/\mu_w}$	Viscous displacement stability	20–100	$M \gg 1$: front unstable; requires fine grid, fingering-corrected k_r, or sub-grid mixing model
Capillary number Ca	$\frac{\mu_i v}{\gamma}$	Viscous vs. capillary forces	10^{-12}–10^{-6}	$\mathrm{Ca} \lesssim 10^{-6}$: capillary-dominated, $p_c(S)$ controls front shape; $\mathrm{Ca} \gtrsim 10^{-4}$: viscous-dominated, capillary smoothing negligible
Gravity number N_g	$\frac{k\Delta\rho g}{\mu_g v}$	Gravity vs. viscous forces	10^{-3}–10^{2}	$N_g \gg 1$: vertical-equilibrium / gravity-current approximation valid; $N_g \ll 1$: full 3D simulation required
Peclet number Pe	$\frac{vL}{D}$	Advection vs. diffusion	10^{-5}–10^{3}	$\mathrm{Pe} \gg 1$: advection-dominated, dispersion model needed; $\mathrm{Pe} \lesssim 1$: diffusion-controlled mixing and dissolution
Bond number Bo	$\frac{\Delta\rho g L^2}{\gamma}$	Gravity vs. capillarity	10^{-5}–10^{2}	$\mathrm{Bo} \ll 1$ at pore scale: capillary trapping effective; $\mathrm{Bo} \gg 1$ at continuum scale: buoyant migration dominates
Knudsen number Kn	$\frac{\lambda}{d_{\mathrm{pore}}}$	Mean free path vs. pore size	10^{-5}–10^{1}	$\mathrm{Kn} < 10^{-3}$: continuum Darcy/-Fick; $10^{-3} < \mathrm{Kn} < 10^{-1}$: Klinkenberg slip correction; $0.1 < \mathrm{Kn} < 10$: dusty-gas model; $\mathrm{Kn} > 10$: Knudsen diffusion

Figure 2 synthesizes the dimensionless analysis by mapping flow regimes in capillary number–mobility ratio space. Hydrogen–brine systems typically operate in the viscous fingering regime due to their high mobility ratios ($M \sim 20$–100), whereas CH_4 and CO_2 systems may achieve more stable displacement under equivalent conditions. This regime map provides practitioners with a diagnostic tool for assessing displacement stability and identifying conditions where operational modifications (reduced injection rates, WAG strategies) may improve sweep efficiency.

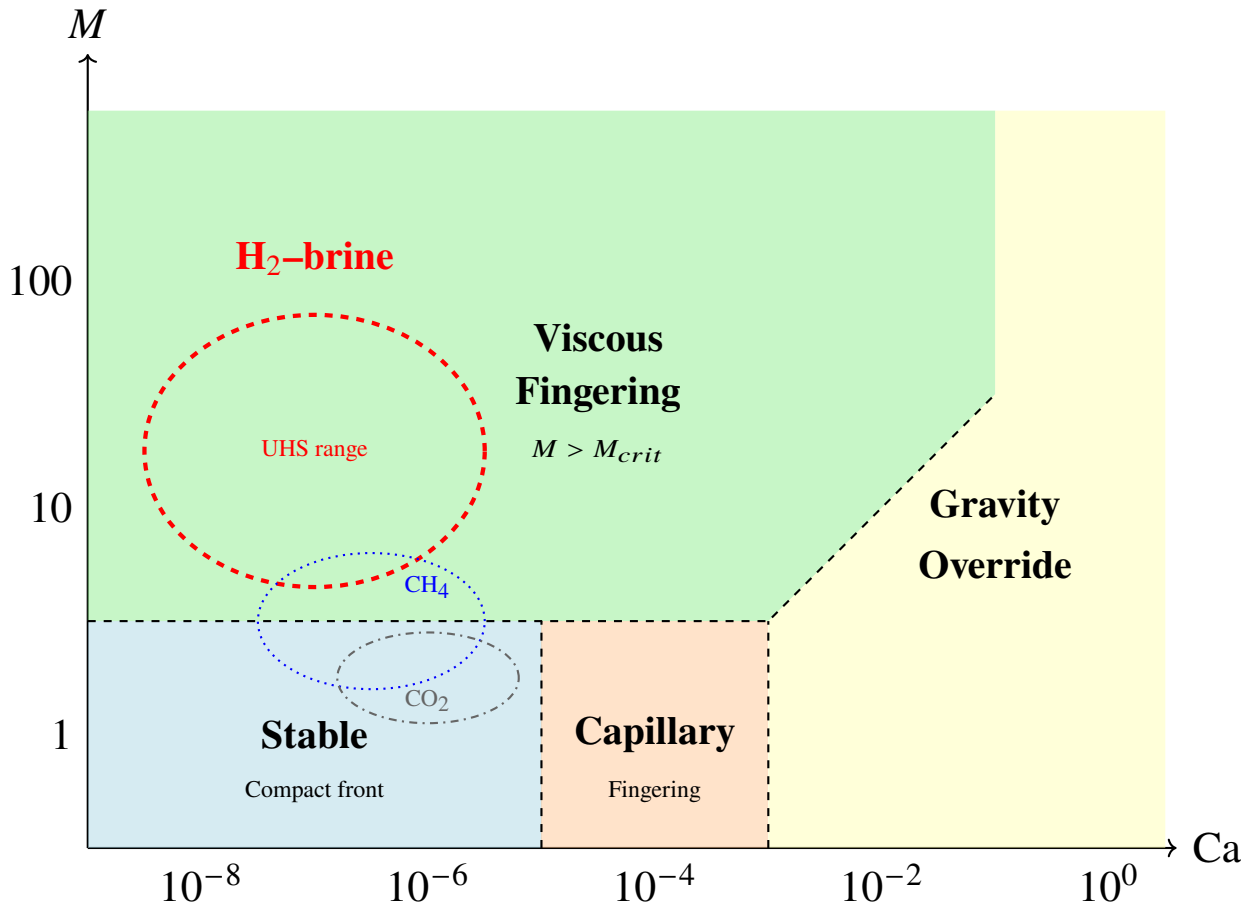


Figure 2. Multiphase flow regime map in capillary number–mobility ratio (Ca–M) space for gas–brine displacement in porous media. Hydrogen–brine systems (red dashed ellipse) typically operate in the viscous fingering regime due to high mobility ratios ($M \sim 20$–100), in contrast to CH_4 and CO_2 systems that may achieve more stable displacement. Regime boundaries are approximate and depend on pore structure and wettability.

3.11 Dimensionless analysis applied: regime classification for representative UHS scenarios

To translate the dimensionless framework of Table 4 into operational guidance, we compute the full set (M, Ca, N_g, Pe, Bo, Kn) for three representative UHS scenarios spanning the geological and operational range encountered in practice. For each scenario we distinguish a near-well regime (high Darcy velocity during active injection or withdrawal) from a far-field regime (low Darcy velocity during quiescent storage), because operational conditions can shift a single reservoir between distinct regions of the flow-regime map.

Scenario A: Depleted sandstone gas reservoir. Conditions: $P = 100$ bar, $T = 323$ K, $k = 100$ mD, grain size $L \sim 200$ μm, pore-throat diameter $d_{\text{pore}} \sim 50$ μm, endpoint $k^0_{r,g} = 0.6$, $k^0_{r,w} = 0.4$, IFT $\gamma = 60$ mN/m. For $\mu_w/\mu_g \approx 55$, the mobility ratio is $M \approx 83$, independent of velocity. At a near-well Darcy velocity $v \sim 10^{-3}$ m/s, the dimensionless numbers are Ca $\approx 1.5 \times 10^{-7}$, $N_g \approx 0.1$, Pe ≈ 40, Bo $\approx 7 \times 10^{-3}$,

Kn $\approx 2 \times 10^{-5}$. At a far-field velocity $v \sim 10^{-6}$ m/s, the same reservoir yields Ca $\approx 1.5 \times 10^{-10}$, $N_g \approx 110$, Pe ≈ 0.04, with Bo and Kn unchanged.

Scenario B: Deep saline aquifer. Conditions: $P = 150$ bar, $T = 343$ K, $k = 10$ mD, $L \sim 100$ μm, $d_{\text{pore}} \sim 20$ μm, endpoint $k^0_{r,g} = 0.5$, $k^0_{r,w} = 0.35$. Mobility ratio $M \approx 79$. Near-well ($v \sim 5 \times 10^{-4}$ m/s): Ca $\approx 7 \times 10^{-8}$, $N_g \approx 0.02$, Pe ≈ 10. Far-field ($v \sim 5 \times 10^{-7}$ m/s): Ca $\approx 7 \times 10^{-11}$, $N_g \approx 22$, Pe ≈ 0.01. Bond number Bo $\approx 1.6 \times 10^{-3}$ and Knudsen number Kn $\approx 4 \times 10^{-5}$ throughout.

Scenario C: Tight reservoir / caprock-adjacent zone. Conditions: $P = 100$ bar, $T = 323$ K, $k = 0.01$ mD, $L \sim 10$ μm, $d_{\text{pore}} \sim 50$ nm, endpoint $k^0_{r,g} = 0.3$, $k^0_{r,w} = 0.25$. Mobility ratio $M \approx 67$. Near-well ($v \sim 10^{-5}$ m/s): Ca $\approx 1.5 \times 10^{-9}$, $N_g \approx 10^{-3}$, Pe ≈ 0.02. Far-field ($v \sim 10^{-8}$ m/s): Ca $\approx 1.5 \times 10^{-12}$, $N_g \approx 1$, Pe $\approx 2 \times 10^{-5}$. Critically, Kn ≈ 0.024 throughout, placing the formation in the slip-flow regime where Klinkenberg corrections are mandatory.

Modeling decisions implied by the analysis

These computations expose three concrete modeling consequences that are obscured when dimensionless numbers are merely tabulated:

1. **The same reservoir occupies different regime regions during different operational phases.** In Scenario A, N_g shifts by three orders of magnitude between near-well injection ($N_g \approx 0.1$, viscous-dominated) and far-field storage ($N_g \approx 110$, gravity-stable). Simulators that apply a single vertical-equilibrium assumption uniformly across the domain will misrepresent either the near-well displacement dynamics or the long-term plume migration. A hybrid formulation, or local grid refinement near the wellbore with vertical-equilibrium upscaling in the far field, is therefore appropriate.
2. **Mobility ratio alone does not determine displacement stability; capillary number sets the regime boundary.** All three scenarios share $M \sim 70$–85, yet Ca varies by five orders of magnitude. In the near-well regime of Scenario A (Ca $\sim 10^{-7}$, $M \sim 83$), the displacement lies in the viscous-fingering region of Figure 2. In the far-field of Scenario C (Ca $\sim 10^{-12}$, $M \sim 67$), the displacement is capillary-dominated despite identical mobility contrast. Constitutive uncertainty in k_r dominates forecast error in the former regime; uncertainty in p_c dominates in the latter. Sensitivity analyses should be designed accordingly.
3. **Knudsen number identifies which formations require non-Darcy corrections.** Scenarios A and B yield Kn $\sim 10^{-5}$, comfortably in the continuum regime where standard Darcy/Fick formulations apply. Scenario C, representative of caprocks and tight reservoir layers, yields Kn ≈ 0.024, requiring Klinkenberg-corrected permeability (Eq. 19). For sub-50-nm pore throats characteristic of shale caprocks, Kn approaches or exceeds 0.1 and the dusty-gas model becomes necessary. This threshold is a hard constraint on caprock integrity assessment: simulations that omit slip corrections will systematically underestimate diffusive and slip-enhanced hydrogen migration through the seal.

The Peclet-number analysis adds a final operational insight. In all three scenarios, far-field Pe values are at or below unity, meaning that long-term mixing, dissolution, and compositional evolution in the storage zone are controlled by molecular diffusion rather than advection. Reservoir simulators that neglect aqueous-phase diffusion of dissolved H_2 (a common approximation) will accurately reproduce active-cycle behavior but may systematically misrepresent the slow compositional drift that determines withdrawal purity over multi-year storage durations.

These worked examples demonstrate that the dimensionless framework is not merely classificatory but operationally prescriptive: each number, evaluated at the relevant scenario, triggers specific modeling choices that propagate directly to forecast reliability.

4 Hydrogen Trapping Mechanisms

The long-term security of underground hydrogen storage depends on multiple trapping mechanisms that immobilize hydrogen or limit its upward migration within the geological formation. Four primary mechanisms are commonly discussed for porous-media UHS: structural trapping, residual trapping, solubility trapping, and (typically negligible) mineral trapping [2, 1, 8]. These mechanisms operate at different spatial and temporal scales with distinct implications for storage capacity, recovery efficiency, and containment.

Figure 3 illustrates the principal mechanisms governing hydrogen retention and loss in underground storage. Structural trapping beneath low-permeability caprocks and residual trapping of disconnected gas ganglia provide the primary security for stored hydrogen. Solubility trapping represents a reversible sink that buffers compositional changes but contributes to mixing losses. Mineral trapping and adsorption are generally minor for H_2 due to its low reactivity and weak surface interactions. Microbial consumption, where present, can be a significant loss pathway. The following subsections quantify each mechanism and its mathematical representation.

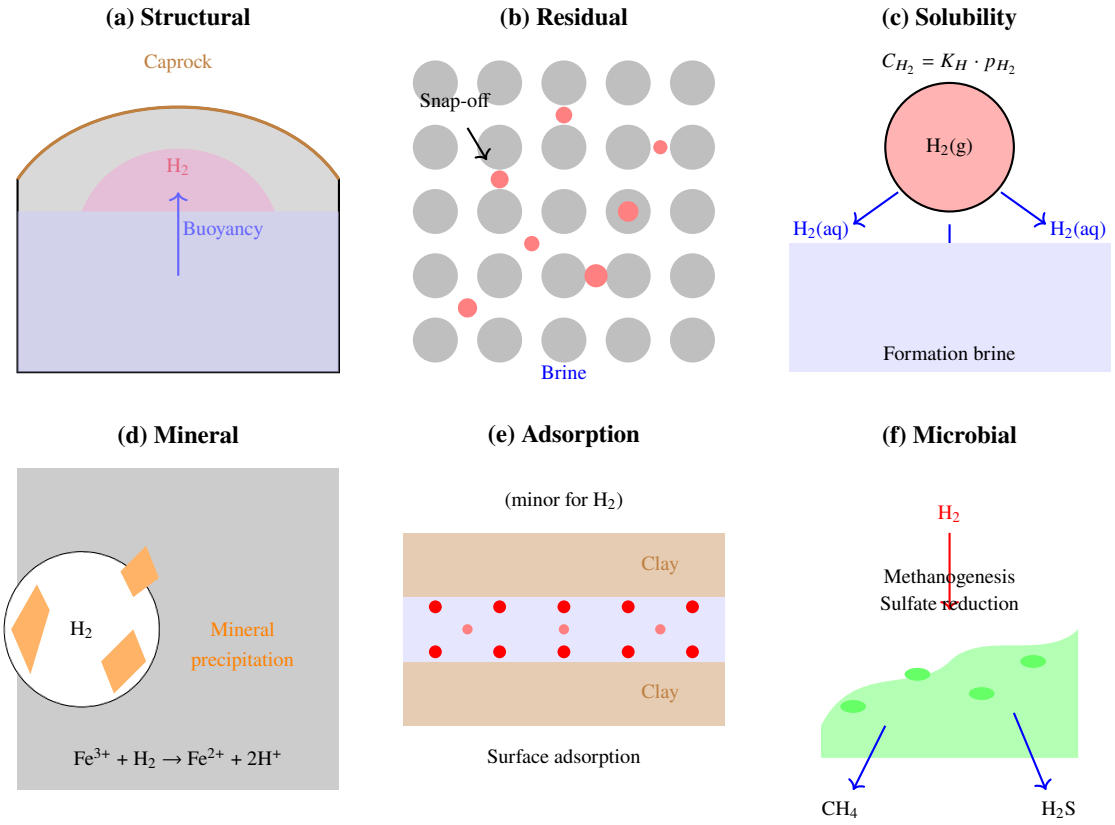


Figure 3. Schematic representation of hydrogen trapping mechanisms in underground storage: (a) structural trapping beneath low-permeability caprock driven by buoyancy; (b) residual trapping of disconnected gas ganglia following snap-off during imbibition; (c) solubility trapping via dissolution into formation brine governed by Henry's law; (d) mineral trapping through geochemical reactions (typically minor for H_2); (e) adsorption on mineral surfaces (minor contribution); (f) microbial consumption converting H_2 to CH_4 or H_2S. Structural and residual trapping dominate storage security; solubility and microbial mechanisms represent loss pathways.

4.1 Structural Trapping

Structural trapping is the primary mechanism for retaining mobile hydrogen within the storage formation. It relies on the accumulation of buoyant gas beneath an impermeable seal (caprock) in a structural closure [1, 2].

The driving force is the density contrast between hydrogen ($\rho_{H_2} \approx 6$–8 kg/m^3 at ~100 bar and 50–60°C) and brine ($\rho_{brine} \approx 1000$–$1200$ kg/m^3), creating buoyancy pressure:

$$\Delta p_{buoy} = (\rho_w - \rho_g) \cdot g \cdot h \tag{11}$$

where h is the hydrogen column height. For a 100-m column, $\Delta p_{buoy} \approx 1$ MPa.

The caprock limits upward migration through its capillary entry pressure, the threshold for gas to penetrate the seal's fine pore network [45]:

$$p_e = \frac{2\gamma \cos\theta}{r_{throat}} \tag{12}$$

For hydrogen ($\gamma \approx 50$–70 mN/m) in typical shale caprocks ($r_{throat} \sim 10$–100 nm), entry pressures are commonly in the MPa range; the corresponding maximum supported column height follows $h_{\max} \approx p_e/[(\rho_w - \rho_g)g]$ and therefore spans from tens to hundreds of meters (or more), depending on wettability and pore-throat size [45]. Structural trapping is typically the *dominant* containment mechanism in structural closures and is largely reversible during withdrawal.

Despite recent progress, hydrogen-specific measurements of wettability and interfacial tension under representative subsurface conditions remain limited compared to CO_2 and CH_4 systems. Hosseini et al. [72] measured H_2–brine interfacial tension over wide ranges of temperatures (298–423 K), pressures (2.76–34.47 MPa), and salinities (0–4.95 mol/kg), finding that γ decreased linearly with increasing pressure and temperature but increased with salinity. Janjua et al. [46] extended these measurements using deionized water, seawater, and various individual brines (NaCl, KCl, $MgCl_2$, $CaCl_2$, Na_2SO_4) at pressures up to 20 MPa and temperatures up to 70°C. For contact angle characterization, Mirchi et al. [48] measured static contact angles of H_2–CH_4 mixtures in contact with brine on oil-wet sandstone and limestone rocks, reporting weakly water-wet behavior with contact angles ranging from 52.4° to 71.1° independent of temperature. Aslannezhad et al. [47] provide a comprehensive synthesis of hydrogen/rock/brine interactions, including the effects of pressure, temperature, salinity, organic contamination, and rock mineralogy on wettability.

Wettability characterization for H_2–brine–rock systems has received increasing attention. Al-Yaseri et al. [76] measured initial and residual trapping of H_2 and N_2 in Fontainebleau sandstone using NMR core flooding, finding comparable trapping behavior between gases. Iglauer et al. [78] and Hashemi et al. [6] reported contact angle measurements indicating that H_2 may exhibit different wetting behavior compared to N_2 or CH_4 on certain mineral surfaces, with implications for capillary trapping predictions. Thaysen et al. [77] used pore-scale imaging to visualize H_2 displacement and trapping, observing that wettability heterogeneity at mineral surfaces influences ganglia morphology and residual saturation.

4.2 Residual Trapping

Residual trapping immobilizes hydrogen as disconnected ganglia during imbibition (brine re-invasion) following drainage [42, 30]. A key pore-scale mechanism is snap-off: as brine advances through gas-filled pore networks, wetting films in pore throats can coalesce, disconnecting gas in adjacent pore bodies from the continuous phase [69, 70].

The Land model [42] provides a commonly used relationship:

$$S_{gr} = \frac{S_{g,max}}{1 + C \cdot S_{g,max}} \tag{13}$$

where S_{gr} is residual gas saturation, $S_{g,max}$ is maximum saturation during preceding drainage, and C is the Land coefficient.

Available measurements for H_2–brine systems suggest Land trapping coefficients in sandstones on the order of $C \approx 1.0$–1.8, with maximum residual gas saturations $S_{gr,\max} \approx 0.18$–0.28, depending on rock type, wettability, and measurement protocol [6, 43]. For comparison, reported CO_2–brine values in sandstone span a similar range, with $C \approx 0.8$–2.0 and $S_{gr,\max} \approx 0.20$–0.35 [30]. Overall, residual trapping provides a

Table 5. Comparison of hydrogen trapping mechanisms [1, 2, 6].

Mechanism	Timescale	Relative Importance	Reversibility	Primary Controls
Structural	Instantaneous	Dominant	Largely reversible	Caprock quality, closure geometry
Residual	Seconds–hours	Secondary	Partially	Pore geometry, wettability, IFT
Solubility	Hours–days	Typically minor–moderate	Reversible	Pressure, temperature, salinity
Mineral	Years–decades	Typically negligible (capacity)	Irreversible	Mineralogy, temperature, biogeochemistry

secondary immobilization mechanism that can improve storage security but may reduce early-cycle hydrogen recoverability, and its magnitude can evolve during cyclic injection/withdrawal as saturation hysteresis stabilizes [6, 30].

4.3 Solubility Trapping

Solubility trapping removes hydrogen from the gas phase by dissolution into formation brine [27, 28]. Hydrogen solubility is commonly described using Henry-type behavior with salting-out corrections:

$$m_{H_2} = K_H(T)\, f_{H_2}\, \exp(-k_s\, m_s) \tag{14}$$

where K_H is the Henry constant, f_{H_2} is fugacity, k_s is the Setschenow coefficient, and m_s is salt molality [29].

At UHS pressures, measured H_2 solubility in NaCl brines is on the order of 10^{-2}–10^{-1} mol/kg$_{H_2O}$, depending on temperature and salinity (e.g., ~0.05–0.07 mol/kg around 10–15 MPa in brines of a few mol/kg NaCl) [27, 11]. Solubility trapping is typically minor–moderate relative to structural and residual mechanisms, but it can contribute to diffusive losses and may provide substrate for microbial activity.

4.4 Mineral Trapping

Mineral trapping (in the sense of long-term, irreversible immobilization as new solid phases) is typically negligible for hydrogen on operational timescales [24, 25]. Nevertheless, geochemical and microbial processes can affect gas quality in site-dependent ways (e.g., sulfur cycling and potential H_2S formation in reactive systems) [24, 25].

4.5 Comparison of Trapping Mechanisms

The dominance of structural trapping underscores the importance of site selection emphasizing structural closure with high-quality seals. Residual trapping provides crucial secondary containment that enhances long-term security but can reduce recoverability.

5 Hydrogen Diffusion and Dissolution

Hydrogen's small molecular size and low molecular mass confer *among the highest* diffusivities of any gas, making diffusive transport a more significant consideration for UHS than for natural gas or CO_2 storage in many settings [1, 49]. This section examines diffusion across transport regimes, from continuum (Fickian) behavior in conventional reservoirs to Knudsen-dominated transport in tight formations and nanoporous seals.

Table 6. Representative hydrogen diffusion coefficients in gas and aqueous phases under conditions relevant to UHS. Gas-phase values decrease with pressure (increased collision frequency). Aqueous-phase values increase with temperature and decrease with salinity. Data compiled from [36, 49, 50].

System	Conditions	D (m^2/s)	Notes
Gas-phase binary diffusion (D_g) at low pressure			
H_2–N_2	1 bar, 25°C	7.8×10^{-5}	Typical 1-bar value
H_2–CH_4	1 bar, 25°C	7.3×10^{-5}	Typical 1-bar value
H_2–CO_2	1 bar, 25°C	6.5×10^{-5}	Typical 1-bar value
Gas-phase diffusion at high pressure (order-of-magnitude estimates)			
H_2 (gas)	100 bar, 50°C	$\sim 10^{-6}$–10^{-7}	Chapman–Enskog scale
H_2 (gas)	200 bar, 80°C	$\sim 10^{-7}$	Chapman–Enskog scale
Aqueous-phase diffusion (D_w), dissolved H_2			
H_2 in pure water	25°C	5.1×10^{-9}	Representative value
H_2 in pure water	50°C	7.0×10^{-9}	Representative value
H_2 in pure water	80°C	1.0×10^{-8}	Representative value
H_2 in 1 M NaCl	25°C	4.5×10^{-9}	Salinity reduces D_w
H_2 in 3 M NaCl	25°C	3.8×10^{-9}	Stronger salinity effect
Scaling relationships			
Gas phase (Chapman–Enskog): $D_g \propto T^{1.75}/P$			
Aqueous phase (Stokes–Einstein form): $D_w \propto T/\mu_w$			

5.1 Molecular Diffusion Fundamentals

The molecular diffusivity of hydrogen is enhanced by its small kinetic diameter ($d_m \approx 0.289$ nm) and low molecular mass ($M = 2.02$ g/mol), which together increase thermal velocities and mean free paths [12, 50]. According to kinetic theory, the binary diffusion coefficient scales as:

$$D_{AB} \propto \frac{T^{3/2}}{P \cdot \sigma_{AB}^2 \cdot \Omega_D} \sqrt{\frac{1}{M_A} + \frac{1}{M_B}}, \tag{15}$$

where σ_{AB} is the collision diameter, Ω_D is the collision integral, and M_A, M_B are molecular weights. The low mass of hydrogen therefore enhances diffusivity compared to heavier molecules.

Table 6 summarizes representative diffusion coefficients for hydrogen in media relevant to UHS. Gas-phase diffusion decreases with pressure (to first order, $\propto 1/P$), whereas aqueous diffusion increases with temperature and decreases with salinity due to increased viscosity/ion effects.

Several important observations emerge from Table 6. First, hydrogen's aqueous diffusivity ($D_w \approx 5$–10×10^{-9} m^2/s) is commonly *a few times higher* than that of methane and CO_2, implying that dissolved hydrogen can spread more rapidly through formation brines. Second, gas-phase diffusion decreases approximately inversely with pressure, so at reservoir pressures (100–200 bar), D_g is reduced by *about two orders of magnitude* relative to 1-bar conditions. Third, salinity reduces aqueous diffusivity by roughly 10–25% over typical formation-brine concentrations.

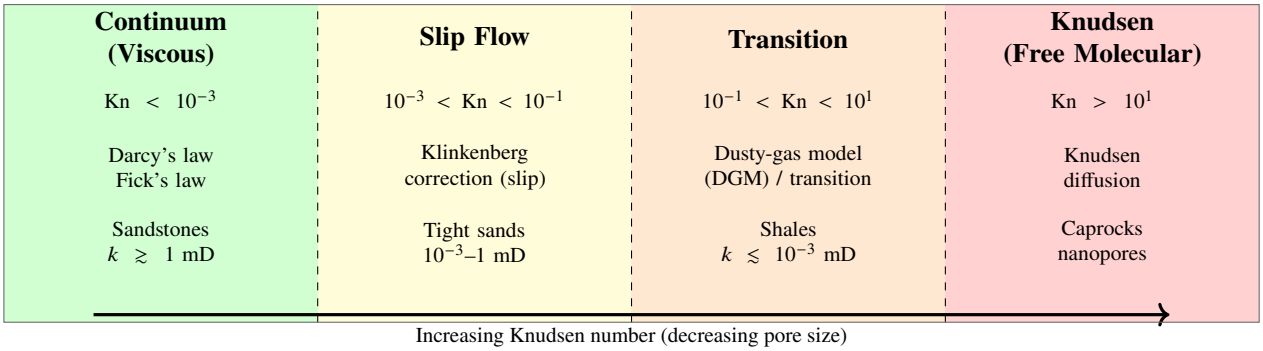


Figure 4. Classification of gas transport regimes by Knudsen number with corresponding models and typical geological formations. Adapted from [51, 52, 55].

5.2 Transport Regime Classification

The appropriate transport model depends on the ratio of molecular mean free path to pore diameter, characterized by the Knudsen number [51, 52]:

$$\mathrm{Kn} = \frac{\lambda}{d_{pore}}. \tag{16}$$

The mean free path is calculated from kinetic theory [50]:

$$\lambda = \frac{k_B T}{\sqrt{2}\,\pi d_m^2 P}, \tag{17}$$

where k_B is Boltzmann's constant, T is temperature, d_m is molecular diameter, and P is pressure. For hydrogen at representative reservoir conditions (100 bar, 350 K), $\lambda \approx 1.3$ nm.

Pore-size scaling analysis. The transition between transport regimes can be expressed as a critical pore diameter at which Kn = 0.1 (onset of slip effects) or Kn = 1 (transition regime):

$$d_{\mathrm{pore}}^{\mathrm{crit}} = \frac{\lambda}{\mathrm{Kn}_{\mathrm{crit}}} = \frac{k_B T}{\sqrt{2}\pi d_m^2 P \cdot \mathrm{Kn}_{\mathrm{crit}}} \tag{18}$$

For hydrogen at 100 bar and 350 K ($\lambda \approx 1.3$ nm): slip effects become significant (Kn > 0.1) when $d_{\mathrm{pore}} < 13$ nm, corresponding to permeabilities below approximately 10^{-18} m^2 (1 nD). The transition regime (Kn ~ 1) occurs at $d_{\mathrm{pore}} \sim 1.3$ nm. These thresholds are approximately 2–3 times larger than for methane due to hydrogen's smaller molecular diameter, meaning that Klinkenberg corrections become relevant at higher permeabilities for H_2 than for CH_4 or CO_2 [52, 55].

Four transport regimes are commonly distinguished based on Knudsen number, as illustrated in Figure 4. For hydrogen at UHS conditions ($\lambda \approx 1.3$ nm), conventional reservoir rocks generally operate in the continuum regime (Kn $\ll$ 1), tight formations may require slip corrections, and nanoporous seals may require dusty-gas or Knudsen diffusion treatment.

Continuum regime (Kn < 0.001): Molecule–molecule collisions dominate over molecule–wall collisions. Standard Darcy flow and Fickian diffusion apply. This is valid when pores are sufficiently large that Kn $\ll$ 1 (typically sub-micron to micron-scale pores at UHS pressures).

Slip flow regime (0.001 < Kn < 0.1): A finite slip velocity exists at pore walls. The Klinkenberg correction to apparent permeability is often required:

$$k_{app} = k_\infty \left(1 + \frac{b}{P}\right), \tag{19}$$

where b is the slip factor. Hydrogen generally exhibits larger slippage than heavier gases due to its smaller molecular size and higher thermal velocity, and b increases strongly as permeability decreases [56, 57].

Transition regime ($0.1 < \mathrm{Kn} < 10$): Both molecule–molecule and molecule–wall collisions are significant. Combined viscous and Knudsen contributions are important, and the dusty-gas model (DGM) provides an accurate framework [53].

Knudsen regime ($\mathrm{Kn} > 10$): Molecule–wall collisions dominate. Transport is controlled by Knudsen diffusion [53]:

$$D_K = \frac{d_{pore}}{3}\sqrt{\frac{8RT}{\pi M}}. \tag{20}$$

For hydrogen, $\sqrt{8RT/(\pi M)}$ is approximately $\sqrt{M_{CH_4}/M_{H_2}} \approx 2.8$ times larger than for methane, enhancing Knudsen diffusion for a given pore size and temperature.

5.2.1 *Practical regime selection criteria.*

For UHS applications, the appropriate transport model can be selected based on formation permeability as a practical proxy for pore size. Table 7 provides selection guidance based on typical Knudsen number ranges. High-permeability reservoir sandstones ($k > 10$ mD) operate in the continuum regime where standard Darcy–Fick formulations apply. Tight reservoir rocks and transition zones (0.001–10 mD) may require Klinkenberg-corrected permeability, particularly for hydrogen. Caprock materials ($k < 0.001$ mD) typically require dusty-gas or effective diffusion models that account for Knudsen effects. When in doubt, the Knudsen number should be calculated explicitly using the definitions of Kn and λ given above, with formation-specific pore-size data from mercury intrusion porosimetry or nitrogen adsorption.

Table 7. Practical regime selection criteria based on formation permeability for hydrogen transport at reservoir conditions (100 bar, 350 K).

Permeability	Typical Kn	Regime	Recommended Model
> 10 mD	< 0.001	Continuum	Darcy + Fick
0.01–10 mD	0.001–0.1	Slip flow	Klinkenberg correction
0.001–0.01 mD	0.1–1	Transition	Dusty-gas model
< 0.001 mD	> 1	Knudsen	Knudsen diffusion

5.3 Effective Diffusion in Porous Media

In porous media, effective diffusion is reduced from molecular values by porosity and pore-network geometry [49]:

$$D_{eff} = D_{mol} \cdot \frac{\phi}{\tau^2}, \tag{21}$$

where ϕ is porosity and τ is tortuosity. The tortuosity factor accounts for the increased path length through the pore network compared to a straight-line distance. For typical reservoir rocks, $\tau \approx 1.5$–3; for tight shales and claystones, $\tau \approx 3$–10 [49]. *(Note: some conventions use $D_{\mathrm{eff}} = D_{\mathrm{mol}}\,\phi/\tau$; here τ is defined such that the reduction scales with τ^2.)*

An alternative formulation uses the Archie cementation exponent [67, 68]:

$$\frac{D_{eff}}{D_{mol}} = \phi^m, \tag{22}$$

with $m \approx 1.8$–2.5 for claystones, providing a convenient correlation for caprock materials.

5.3.1 *Scale-dependence of effective diffusion.*

Effective diffusion coefficients exhibit significant scale-dependence that must be considered when translating laboratory measurements to field-scale predictions. At the pore scale, molecular diffusion operates with

Table 8. Representative *effective* diffusion coefficients reported for hydrogen in clay-rich sealing rocks and related geomaterials.

Material / context	Method / state	D_{eff} (m^2/s)	Notes
Boom Clay	Dissolved H_2, sterilisation protocol (parallel to bedding)	$(5.4–7.5)\times10^{-10}$	First H_2 diffusion experiments reported for Boom Clay (parallel to bedding) [64].
Boom Clay	Dissolved H_2 in saturated Boom Clay (anisotropic)	$(2.64–7.25)\times10^{-10}$	Jacops et al. report 2.64×10^{-10} (perpendicular to bedding) and $5.51–7.25\times10^{-10}$ (parallel bedding) [59].
Clay/claystone (literature context)	Water-saturated, very low values reported	$\sim 3\times10^{-11}$	Low-end values reported in the literature database context [58].
Opalinus Clay (whole-rock plug)	Breakthrough-type diffusion on intact plug (original vs wetted)	$(1.2–1.8)\times10^{-9}$	1.8×10^{-9} (original), 1.2×10^{-9} (wetted) [58].
Rock salt (whole-rock plug)	Breakthrough-type diffusion (original vs wetted)	$(1.4\times10^{-9}–1.3\times10^{-8})$	Strong wetting effect: 1.3×10^{-8} (original) vs 1.4×10^{-9} (wetted) [58].

coefficients of order 10^{-9} m^2/s in the aqueous phase and 10^{-5}–10^{-7} m^2/s in the gas phase depending on pressure. At the core scale (cm), tortuosity and constrictivity reduce effective diffusivity by factors of 2–10, yielding $D_{eff} = D_{mol} \cdot \phi/\tau^2$ where τ typically ranges from 2–5 for sandstones and 5–15 for shales [49]. At the reservoir scale (m–km), additional factors emerge: macroscopic heterogeneity creates preferential diffusion pathways through higher-porosity layers; mechanical dispersion from residual flow augments effective spreading; and fracture networks in caprocks may provide fast diffusion conduits with orders-of-magnitude higher effective coefficients than the intact matrix [1]. For caprock integrity assessment, laboratory-measured D_{eff} values should be considered lower bounds, with sensitivity analysis exploring enhancement factors of 2–10 to account for sub-resolution heterogeneity and potential fracture contributions. Field-scale effective diffusivities inferred from tracer tests or production data may exceed core-scale values by factors of 3–30 depending on formation heterogeneity [49, 58].

5.4 Caprock Diffusion and Leakage Assessment

Diffusive hydrogen loss through caprocks represents a potential long-term containment concern. Table 8 therefore compiles representative effective diffusion coefficients reported for hydrogen in sealing rocks, while explicitly distinguishing between (i) through-diffusion of dissolved H_2 in fully water-saturated clay-rich media and (ii) whole-rock plug (breakthrough/permeation) tests that may involve partially dry conditions and/or microcrack effects. As a result, published D_{eff} values span orders of magnitude and depend not only on mineralogy, porosity, and anisotropy, but also strongly on saturation state and measurement protocol [58, 59].

The steady-state diffusive flux through a caprock of thickness h is [36]:

$$J_{diff} = D_{eff}\,\frac{C_{res} - C_{above}}{h} \;\approx\; D_{eff}\,\frac{C_{res}}{h}, \tag{23}$$

where C_{res} is the dissolved hydrogen concentration at the reservoir–caprock interface (controlled by solubility at storage pressure) and C_{above} is often taken as negligible for a conservative estimate.

As an illustrative upper-bound calculation, consider a 50-m thick clay-rich caprock with $D_{eff} = 5\times10^{-11}$ m^2/s, $C_{res} = 0.05$ mol/L (50 mol/m^3), and an areal extent of 1 km^2. The resulting steady-state annual diffusive loss is:

$$\dot{n} = \left(D_{eff}\,\frac{C_{res}}{h}\right) A \;\approx\; 5\times10^{-5}\ \text{mol/s}$$

which corresponds to $\approx 1.6 \times 10^3$ mol/yr, i.e. ≈ 3 kg H_2/yr. Note that steady state over $h = 50$ m implies a very long diffusion timescale ($t \sim h^2/D_{eff}$), so this estimate represents a conservative long-term upper bound; project-timescale losses would typically be smaller.

The same upper-bound calculation can be performed for CH_4 and CO_2 through an identical caprock to give a quantitative ordering of diffusive losses across the three gases relevant to subsurface storage. Using aqueous-phase diffusivities $D_{H_2} = 5 \times 10^{-9}$, $D_{CH_4} = 1.5 \times 10^{-9}$, $D_{CO_2} = 1.9 \times 10^{-9}$ m^2/s, dissolved-phase concentrations at the reservoir–caprock interface of $C_{H_2} = 50$ mol/m^3 (Eq. 14 with Henry constant for H_2 at 100 bar, 50°C), $C_{CH_4} \approx 12$ mol/m^3, $C_{CO_2} \approx 1200$ mol/m^3 (reflecting the very high CO_2 solubility in brine), and the same caprock geometry (50 m thickness, 1 km^2 areal extent, identical tortuosity factor), the steady-state annual losses are: H_2 ($\approx 1.6 \times 10^3$ mol/yr ≈ 3 kg/yr, as computed above). CH_4 ($\approx 1.1 \times 10^2$ mol/yr ≈ 1.8 kg/yr). CO_2 ($\approx 1.4 \times 10^4$ mol/yr ≈ 630 kg/yr). Three observations follow from this comparison. First, on a per-kg basis CO_2 diffusive loss exceeds H_2 by roughly two orders of magnitude through the same caprock, driven by the much higher CO_2 solubility in brine. The widely held intuition that "H_2 leaks faster because the molecule is smaller" is not supported by this analysis: the relevant transport in a water-saturated clay caprock is aqueous-phase diffusion of the dissolved gas, and the controlling parameter is solubility × diffusivity rather than kinetic diameter. Second, CH_4 losses are smaller than H_2 losses, despite CH_4 being the historical analog used to justify caprock integrity for hydrogen storage; the conservative direction of this difference (less than 2×) does not invalidate the analog but does indicate that historical CH_4 storage data slightly underestimate H_2 diffusive losses. Third, the absolute H_2 loss rate (~3 kg/yr per km^2) is a small fraction of the stored mass for any commercial UHS facility (typically 10^7–10^8 kg), so this loss pathway is not first-order for inventory accounting; its significance is for the cumulative environmental flux and for caprock-integrity assessment under conditions where measured D_{eff} approaches the upper end of the four-orders-of-magnitude range discussed in §9.4.4.

Despite growing recognition that diffusive losses through caprocks may significantly impact long-term UHS integrity, experimental characterization of hydrogen transport in seal formations remains methodologically fragmented. Reported effective diffusion coefficients for H_2 in shale and clay caprocks span approximately four orders of magnitude, from 1×10^{-11} to 1×10^{-7} m^2/s [60, 61, 62], reflecting differences in sample preparation, measurement technique, and environmental conditions. Using a dynamic gravimetric vapor sorption system on samples from two natural gas storage caprocks at 45°C, Salina Borello et al. [60] measured hydrogen diffusion coefficients in the range 1×10^{-10} to 6×10^{-8} m^2/s, with wet samples exhibiting values approximately two times lower than dry samples. Yang et al. [61] employed a novel through-diffusion apparatus on Eagle Ford and Wolfcamp shales under dry conditions, obtaining effective diffusivities of 2.51×10^{-8} to 9.85×10^{-8} m^2/s, and demonstrated that pore network connectivity (characterized by hysteresis in N_2 physisorption) exerts stronger control on diffusion behavior than total porosity. Earlier work by Michelsen et al. [62] on water-saturated caprock cores yielded substantially lower values of 8.0×10^{-11} to 1.8×10^{-10} m^2/s, underscoring the critical influence of saturation state. A semi-analytical framework developed by Ghaedi et al. [63] relates cumulative hydrogen loss to the square root of time and identifies caprock porosity, gas saturation, and diffusion coefficient as governing parameters; notably, the presence of residual hydrocarbon gas in the caprock can facilitate H_2 diffusion by modifying chemical potential gradients.

5.4.1 Effective medium approximations for tight caprocks.

In tight caprocks where multiple transport mechanisms operate simultaneously, effective medium theory provides a framework for combining contributions. The dusty-gas model (DGM) [53] treats the porous medium as a collection of stationary "dust" particles and derives transport equations that naturally couple viscous flow, Knudsen diffusion, and ordinary (Stefan–Maxwell) diffusion. In the DGM framework, the total molar flux of species i arises from three contributions: (1) a viscous (Darcy/Poiseuille) term driven by the total pressure gradient, (2) Knudsen diffusion reflecting molecule–wall collisions, and (3) Stefan–Maxwell diffusion representing molecule–molecule interactions. The relative importance of each mechanism depends on the Knudsen number. For hydrogen in clay-rich caprocks (Kn ~ 0.1–10), both Knudsen and molecular

diffusion contribute comparably, and neither pure Fick's law nor pure Knudsen diffusion adequately describes transport. For practical estimates when full DGM calculations are not warranted, the Bosanquet interpolation formula provides a simple harmonic-mean combination of Knudsen and molecular diffusion resistances [54]:

$$\frac{1}{D_{\text{eff}}} = \frac{1}{D_K} + \frac{1}{D_{mol}^{\text{eff}}} \tag{24}$$

where D_K is the Knudsen diffusion coefficient and $D_{mol}^{\text{eff}} = D_{mol}\phi/\tau^2$ is the effective molecular diffusion coefficient accounting for porosity ϕ and tortuosity τ. This approximation correctly recovers the limiting behaviors: $D_{\text{eff}} \to D_K$ when Kn $\gg 1$ (molecule–wall collisions dominate) and $D_{\text{eff}} \to D_{mol}^{\text{eff}}$ when Kn $\ll 1$ (molecule–molecule collisions dominate).

5.4.2 Timescale competition between diffusive and advective transport.

Containment assessment requires comparing diffusive and advective leakage timescales [36]. The characteristic diffusion time across a caprock of thickness h is:

$$t_{diff} = \frac{h^2}{D_{eff}} \tag{25}$$

For a 50-m caprock with $D_{eff} = 10^{-10}$ m^2/s, $t_{diff} \approx 800$ years—indicating that steady-state diffusive profiles develop very slowly relative to operational timescales. In contrast, advective transport through fractures or high-permeability pathways operates on much shorter timescales. The advective transit time through a pathway of length L with Darcy velocity v is:

$$t_{adv} = \frac{L\phi}{v} = \frac{L\phi\mu}{k\Delta p/L} = \frac{L^2\phi\mu}{k\Delta p} \tag{26}$$

For a fracture with $k = 10^{-12}$ m^2, $\phi = 0.01$, $\mu = 10^{-5}$ Pa·s, $L = 50$ m, and $\Delta p = 1$ MPa, $t_{adv} \approx 0.025$ years (9 days). The ratio t_{diff}/t_{adv} thus indicates whether diffusion or advection dominates leakage. For intact caprocks this ratio is much greater than unity and diffusion controls; for fractured or faulted seals the ratio drops well below unity and advective pathways dominate, necessitating different monitoring and mitigation strategies.

6 Thermal Effects

Temperature variations during UHS operations arise from (i) Joule–Thomson heating/cooling during throttling and pressure changes, (ii) injection of gas at temperatures different from the reservoir, and (iii) conductive heat exchange with surrounding formations. These thermal effects can influence gas properties (density, viscosity, solubility), multiphase flow near the well, and potentially microbial activity and geomechanical response [65, 66].

6.1 Joule–Thomson Behavior of Hydrogen

The Joule–Thomson coefficient describes the temperature change during isenthalpic expansion:

$$\mu_{JT} = \left(\frac{\partial T}{\partial P}\right)_H = \frac{1}{C_p}\left[T\left(\frac{\partial V}{\partial T}\right)_P - V\right]. \tag{27}$$

For most gases under ambient and reservoir conditions, $\mu_{JT} > 0$ (throttling causes cooling). Hydrogen is anomalous: above its inversion line, $\mu_{JT} < 0$, so throttling causes *warming* [15]. As a quantitative reference point, hydrogen at ~300 K and near-atmospheric pressure has $\mu_{JT} \approx -0.03$ K/bar [15]. The magnitude remains small at elevated pressures, implying only modest temperature changes for typical UHS drawdowns.

The practical implications are therefore counterintuitive but limited in magnitude:

- **During withdrawal (pressure drop/throttling)**: hydrogen tends to *warm*. As an order-of-magnitude estimate, a 100-bar pressure reduction may produce only a few degrees of warming (e.g. ~4°C) [15].
- **During injection (pressure increase)**: hydrogen tends to *cool* under isenthalpic compression/throttling (same sign reversal).

This behavior contrasts with methane/natural gas, which typically exhibits a positive μ_{JT} (cooling upon pressure drop) of order 0.4–0.5 K/bar at ~300 K and low-to-moderate pressures [15].

6.2 Injection Temperature Effects

More significant temperature perturbations often arise from injecting hydrogen at a temperature different from the reservoir. Depending on surface compression, pipeline heat exchange, and pressure regulation, injection temperatures can deviate from reservoir temperature by *tens of kelvin* in some operations [66, 26].

The characteristic thermal penetration depth associated with conductive diffusion scales as [20]:

$$r_{th} \approx \sqrt{4\alpha_{th}t}, \tag{28}$$

where $\alpha_{th} = \lambda_{th}/(\rho c)_m$ is the effective thermal diffusivity of the saturated rock, typically 5×10^{-7} to 2×10^{-6} m^2/s for sedimentary reservoir rocks [44].

6.3 Thermal Effects on Physical Processes

Temperature variations affect multiple aspects of UHS performance. Gas viscosity increases with temperature, while density follows $\rho \propto P/(ZT)$, and aqueous solubility of H_2 generally decreases with increasing temperature [27, 4]. Gas-phase diffusion increases strongly with temperature (Chapman–Enskog scaling), enhancing mixing at elevated temperatures.

Microbial activity is also temperature-sensitive. In depleted gas fields, microbial risk and hydrogen consumption potential are typically highest at low temperatures (e.g. < 55°C), while risk decreases substantially at higher temperatures (e.g. > 90°C) and may be negligible at sufficiently high reservoir temperatures [7, 14].

7 Conclusions and Outlook

This first part of a two-part review has synthesized the fundamental physics governing hydrogen flow, displacement, trapping, diffusion, and thermal behavior in underground storage systems. The key findings are:

Multiphase Flow and Displacement. Hydrogen's low viscosity creates mobility ratios ($M \sim 20$–100) substantially higher than those for CH_4 ($M \sim 15$–30) or CO_2 ($M \sim 2$–15), making viscous fingering and unstable displacement intrinsic challenges for UHS. Fractional flow analysis reveals that hydrogen fronts are more susceptible to gravity override and early breakthrough. Dimensionless scaling using capillary number (N_c), gravity number (N_g), Bond number (Bo), and Peclet number (Pe) provides a framework for classifying displacement regimes and selecting appropriate modeling approaches.

Trapping Mechanisms. Structural trapping remains the primary containment mechanism at field scale. Residual trapping, governed by Land-type hysteresis models with coefficients $C \approx 1.5$–4 for hydrogen–brine systems, determines the fraction of injected gas immobilized after each withdrawal cycle. Solubility trapping is limited by hydrogen's low solubility in brine (~0.8–1.6 mol/kg at typical reservoir conditions). Mineral trapping through hydrogen consumption in redox reactions is generally negligible over operational timescales but may contribute over geological time.

Diffusive Transport. Hydrogen diffusion in porous media spans multiple regimes depending on the Knudsen number: continuum Fickian diffusion (Kn < 0.01) in reservoir rocks, transitional slip diffusion (0.01 < Kn < 10) in tight formations, and Knudsen diffusion (Kn > 10) in nanoporous caprocks. Effective diffusion coefficients vary over nearly four orders of magnitude (10^{-11}–10^{-7} m^2/s) depending on rock type, porosity, tortuosity, and saturation state.

Thermal Effects. Joule–Thomson cooling during hydrogen expansion is modest ($\mu_{JT} \approx -0.03$ to +0.05 K/bar depending on conditions) but can affect near-wellbore processes during high-rate withdrawal. Thermal effects on viscosity, diffusivity, and phase behavior should be incorporated in non-isothermal simulations.

Research Priorities. Key gaps identified include: (i) systematic experimental data on hydrogen–brine interfacial properties (IFT, contact angles) under full reservoir conditions; (ii) consistent methodologies for caprock diffusion measurement; (iii) extended cycling experiments (>100 cycles) to constrain hysteresis evolution; and (iv) validation against field-scale pilot data.

Next work the constitutive models needed to parameterize these physical processes (relative permeability and capillary pressure correlations), geochemical and microbial interactions that may consume stored hydrogen, geomechanical considerations for cyclic operations, and field-scale implementation challenges.

Funding

This research received no external funding.

Conflict of Interest

The author declares no conflict of interest.

Data Availability Statement

No new data were generated in this review. All data discussed are available in the cited references.

AI Use Declaration

The author used Claude (Anthropic) to support manuscript organization and formatting. The output was critically reviewed, revised where necessary, and verified by the author. The author accepts full responsibility for the accuracy, integrity, and originality of the final manuscript.

Editorial Disclosure

Mohamed F. El-Amin is the Editor-in-Chief of Intelligent Computing for Energy and Environment (ICEE). In accordance with the journal's editorial conflict-of-interest policy, Mohamed F. El-Amin had no involvement in the handling, peer review, or editorial decision of this manuscript. The submission was managed independently by Jisheng Kou and Badre Bossoufi (=), who oversaw the peer-review process and made the editorial decision.

==========

References

[1] N. Heinemann, J. Alcalde, J.M. Miocic, S.J.T. Hangx, J. Kallmeyer, C. Ostertag-Henning, A. Hassanpouryouzband, E.M. Thaysen, G.J. Strobel, C. Schmidt-Hattenberger, K. Edlmann, M. Wilkinson, M. Bentham, R.S. Haszeldine, R. Carbonell, A. Rudloff, Enabling large-scale hydrogen storage in porous media, the scientific challenges, Energy Environ. Sci. 14 (2021) 853–864. https://doi.org/10.1039/D0EE03536J.

[2] D. Zivar, S. Kumar, and J. Foroozesh, Underground hydrogen storage: A comprehensive review, Int. J. Hydrogen Energy 46 (2021) 23436–23462. https://doi.org/10.1016/j.ijhydene.2020.08.138.

[3] R. Tarkowski and B. Uliasz-Misiak, Towards underground hydrogen storage: A review of barriers, *Renew. Sustain. Energy Rev.* 162 (2022) 112451. https://doi.org/10.1016/j.rser.2022.112451.

[4] A. Raza, M. Arif, G. Glatz, M. Mahmoud, M. Al Kobaisi, S. Alafnan, and S. Iglauer, A holistic overview of underground hydrogen storage: Influencing factors, current understanding, and outlook, *Fuel* 330 (2022) 125636. https://doi.org/10.1016/j.fuel.2022.125636.

[5] D. W. Breck, *Zeolite Molecular Sieves: Structure, Chemistry, and Use*, John Wiley & Sons, New York, 1974.

[6] L. Hashemi, M. Blunt, and H. Hajibeygi, Pore-scale modelling and sensitivity analyses of hydrogen-brine multiphase flow in geological porous media, Sci. Rep. 11 (2021) 8348. https://doi.org/10.1038/s41598-021-87490-7.

[7] E. M. Thaysen, S. McMahon, G. J. Strobel, I. B. Butler, N. Heinemann, B. Ngwenya, M. Wilkinson, A. Hassanpouryouzband, C. McDermott, and K. Edlmann, Estimating microbial growth and hydrogen consumption in hydrogen storage in porous media, Renewable and Sustainable Energy Reviews, 151 (2021) 111481. https://doi.org/10.1016/j.rser.2021.111481.

[8] N. S. Muhammed, B. Haq, D. Al Shehri, A. Al-Ahmed, M. M. Rahman, and E. Zaman, A review on underground hydrogen storage: Insight into geological sites, influencing factors and future outlook, Energy Reports 8 (2022) 461–499. https://doi.org/10.1016/j.egyr.2021.12.002.

[9] E. R. Okoroafor, S. D. Saltzer, and A. R. Kovscek, Toward underground hydrogen storage in porous media: Reservoir engineering insights, Int. J. Hydrogen Energy, 47 (2022) 33781–33802. https://doi.org/10.1016/j.ijhydene.2022.07.239.

[10] S.R. Thiyagarajan, H. Emadi, A. Hussain, P. Patange, and M. Watson, A comprehensive review of the mechanisms and efficiency of underground hydrogen storage, *J. Energy Storage* 51 (2022) 104490. https://doi.org/10.1016/j.est.2022.104490.

[11] G.A. Torín-Ollarves and J.P.M. Trusler, Solubility of hydrogen in sodium chloride brine at high pressures, *Fluid Phase Equilib.* 539 (2021) 113025. https://doi.org/10.1016/j.fluid.2021.113025.

[12] J. O. Hirschfelder, C. F. Curtiss, and R. B. Bird, *Molecular Theory of Gases and Liquids*, John Wiley & Sons, New York, 1964.

[13] M. Lysyy, M. Fernø, and G. Ersland, Seasonal hydrogen storage in a depleted oil and gas field, Int. J. Hydrogen Energy, 46(49) (2021) 25160–25174. https://doi.org/10.1016/j.ijhydene.2021.05.030.

[14] E.M. Thaysen, T. Armitage, L. Slabon, A. Hassanpouryouzband, and K. Edlmann, Microbial risk assessment for underground hydrogen storage in porous rocks, *Fuel* 352 (2023) 128852. https://doi.org/10.1016/j.fuel.2023.128852.

[15] DGC (Danish Gas Technology Centre), *Joule–Thomson effect in case of mixtures of natural gas and hydrogen*, DGC note, Oct. 13, 2022. Available at: https://dgc.dk/media/55ufksdg/jt_hydrogen_ng_mix.pdf

[16] D. E. Munson and P. R. Dawson, Constitutive Model for the Low Temperature Creep of Salt (with Application to WIPP), Sandia National Laboratories, Albuquerque, NM, Report SAND79-1853, 1979.

[17] P. Bérest, B. Brouard, M. Karimi-Jafari, and L. Van Sambeek, Transient behavior of salt caverns, Interpretation of mechanical integrity tests, Int. J. Rock Mech. Min. Sci. 44(5) (2007) 767–786. https://doi.org/10.1016/j.ijrmms.2006.11.007.

[18] M. Panfilov, "Underground and pipeline hydrogen storage," in *Compendium of Hydrogen Energy, Vol. 2: Hydrogen Storage, Distribution and Infrastructure*, ed. R. B. Gupta, A. Basile, and T. N. Veziroğlu, Elsevier, 2016, pp. 91–115. https://doi.org/10.1016/B978-1-78242-362-1.00004-3.

[19] N. Heinemann, M. G. Booth, R. S. Haszeldine, M. Wilkinson, J. Scafidi, and K. Edlmann, Hydrogen storage in porous geological formations, Onshore play opportunities in the Midland Valley (Scotland, UK), Int. J. Hydrogen Energy, 43 (2018) 20861–20874. https://doi.org/10.1016/j.ijhydene.2018.09.149.

[20] E. Marín, Characteristic dimensions for heat transfer, *Latin-American Journal of Physics Education* 4(1) (2010) 56–60. Available at: https://www.lajpe.org/jan10/10_Marin.pdf

[21] F. Feldmann, B. Hagemann, L. Ganzer, and M. Panfilov, Numerical simulation of hydrodynamic and gas mixing processes in underground hydrogen storages, Environ. Earth Sci. 75 (2016) 1165. https://doi.org/10.1007/s12665-016-5948-z.

[22] G. Wang, G. Pickup, K. Sorbie, and E. Mackay, Numerical modelling of H_2 storage with cushion gas of CO_2 in subsurface porous media: Filter effects of CO_2 solubility, Int. J. Hydrogen Energy, 47(67) (2022) 28956–28968. https://doi.org/10.1016/j.ijhydene.2022.06.201.

[23] L. Zeng, R. Sander, Y. Chen, Q. Xie, Hydrogen Storage Performance During Underground Hydrogen Storage in Depleted Gas Reservoirs: A Review, *Engineering* 40 (2024) 211–225. https://doi.org/10.1016/j.eng.2024.03.011.

[24] A. Hassanpouryouzband, K. Adie, T. Cowen, E. M. Thaysen, N. Heinemann, I. B. Butler, M. Wilkinson, and K. Edlmann, Geological Hydrogen Storage: Geochemical Reactivity of Hydrogen with Sandstone Reservoirs, ACS Energy Letters, 7 (2022) 2203–2210. https://doi.org/10.1021/acsenergylett.2c01024.

[25] L. Truche, G. Berger, C. Destrigneville, D. Guillaume, and E. Giffaut, Kinetics of pyrite to pyrrhotite reduction by hydrogen in calcite buffered solutions between 90 and 180 °C: Implications for nuclear waste disposal, Geochimica et Cosmochimica Acta, 74 (2010) 2894–2914. https://doi.org/10.1016/j.gca.2010.02.027.

[26] F. Möller, A. Liebscher, S. Martens, C. Schmidt-Hattenberger, and M. Streibel, Injection of CO_2 at ambient temperature conditions, Pressure and temperature results of the "cold injection" experiment at the Ketzin pilot site, Energy Procedia, 63 (2014) 6289–6297. https://doi.org/10.1016/j.egypro.2014.11.660.

[27] S. Chabab, P. Théveneau, C. Coquelet, J. Corvisier, and P. Paricaud, Measurements and predictive models of high-pressure H_2 solubility in brine (H_2O + NaCl) for underground hydrogen storage application, Int. J. Hydrogen Energy, 45 (2020) 32206–32220. https://doi.org/10.1016/j.ijhydene.2020.08.192.

[28] C. Lopez-Lazaro, P. Bachaud, I. Moretti, and N. Ferrando, Predicting the phase behavior of hydrogen in NaCl brines by molecular simulation for geological applications, BSGF – Earth Sciences Bulletin, 190 (2019) 7. https://doi.org/10.1051/bsgf/2019008.

[29] D. Li, C. Beyer, and S. Bauer, A unified phase equilibrium model for hydrogen solubility and solution density, Int. J. Hydrogen Energy, 43(1) (2018) 512–529. https://doi.org/10.1016/j.ijhydene.2017.07.228.

[30] S. Krevor, M.J. Blunt, S.M. Benson, C.H. Pentland, C.A. Reynolds, A.H. Al-Menhali, and B. Niu, Capillary trapping for geologic carbon dioxide storage—from pore scale physics to field scale implications, *Int. J. Greenhouse Gas Control* 40 (2015) 221–237. https://doi.org/10.1016/j.ijggc.2015.04.006.

[31] S.E. Buckley, M.C. Leverett, Mechanism of fluid displacement in sands, Trans. AIME 146 (1942) 107–116.

[32] J. Wang, Y. Yang, S. Cai, J. Yao, Q. Xie, Pore-scale modelling on hydrogen transport in porous media: Implications for hydrogen storage in saline aquifers, Int. J. Hydrogen Energy 48(37) (2023) 13922–13933. https://doi.org/10.1016/j.ijhydene.2022.11.299.

[33] G. P. Benham, J. A. Neufeld, and A. W. Woods, Axisymmetric gravity currents in anisotropic porous media, J. Fluid Mech. 952 (2022) A23. https://doi.org/10.1017/jfm.2022.922.

[34] E. R. Anderman and M. C. Hill, MODFLOW-2000, The U.S. Geological Survey Modular Ground-Water Model— Documentation of Effective-Porosity Parameters in the Advective-Transport Observation (ADV2) Package, U.S. Geological Survey (Denver, CO), 2003 (revised 2005).

[35] A. Sainz-Garcia, E. Abarca, V. Rubi, and F. Grandia, Assessment of feasible strategies for seasonal underground hydrogen storage in a saline aquifer, *Int. J. Hydrogen Energy* 42(26) (2017) 16657–16666. https://doi.org/10.1016/j.ijhydene.2017.05.076.

[36] E. L. Cussler, Diffusion: Mass Transfer in Fluid Systems, 3rd ed., Cambridge University Press, 2009.

[37] T. R. Marrero and E. A. Mason, Gaseous diffusion coefficients, J. Phys. Chem. Ref. Data 1 (1972) 3–118. (NIST reprint, 2009).

[38] R. Lenormand, E. Touboul, and C. Zarcone, Numerical models and experiments on immiscible displacements in porous media, J. Fluid Mech., 189 (1988) 165–187. https://doi.org/10.1017/S0022112088000953.

[39] M. Lysyy, G. Ersland, and M. Fernø, Pore-scale dynamics for underground porous media hydrogen storage, Adv. Water Resour. 163 (2022) 104167. https://doi.org/10.1016/j.advwatres.2022.104167.

[40] T. Ren, X. Shen, and F. Zhang, Numerical analysis of hydrogen fingering in underground hydrogen storage, *Journal of Rock Mechanics and Geotechnical Engineering* 18 (2026) 265–277. https://doi.org/10.1016/j.jrmge.2025.04.015.

[41] G.M. Homsy, Viscous fingering in porous media, Annu. Rev. Fluid Mech. 19 (1987) 271–311. https://doi.org/10.1146/annurev.fl.19.010187.001415.

[42] C. S. Land, Calculation of Imbibition Relative Permeability for Two- and Three-Phase Flow From Rock Properties, SPE Journal 8(2) (1968) 149–156. https://doi.org/10.2118/1942-PA.

[43] Z. Jangda, H. Menke, A. Busch, S. Geiger, T. Bultreys, H. Lewis, and K. Singh, Pore-Scale Visualization of Hydrogen Storage in a Sandstone at Subsurface Pressure and Temperature Conditions: Trapping, Dissolution and Wettability, J. Colloid Interface Sci. 629(Part B) (2023) 316–325. https://doi.org/10.1016/j.jcis.2022.09.082.

[44] J.-Q. Zhang and C.-Q. Zhu, Analysis of thermal properties of main sedimentary rocks in the Beijing area, Unconventional Resources, 4 (2024) 100104. https://doi.org/10.1016/j.uncres.2024.100104.

[45] S. Iglauer, Optimum geological storage depths for structural H_2 geo-storage, J. Petr. Sci. Eng. 212 (2022) 109498. https://doi.org/10.1016/j.petrol.2021.109498.

[46] A. N. Janjua, M. Ali, M. Murtaza, S. Patil, M. S. Kamal, Effects of salinity, temperature, and pressure on H_2–brine interfacial tension: Implications for underground hydrogen storage, J. Energy Storage 95 (2024) 112510. https://doi.org/10.1016/j.est.2024.112510.

[47] M. Aslannezhad, M. Ali, A. Kalantariasl, M. Sayyafzadeh, Z. You, S. Iglauer, A. Keshavarz, A review of hydrogen/rock/brine interaction: Implications for Hydrogen Geo-storage, Prog. Energy Combust. Sci. 95 (2023) 101066. https://doi.org/10.1016/j.pecs.2022.101066.

[48] V. Mirchi, M. Dejam, V. Alvarado, Interfacial tension and contact angle measurements for hydrogen–methane mixtures/brine/oil-wet rocks at reservoir conditions, Int. J. Hydrogen Energy 47(82) (2022) 34963–34975. https://doi.org/10.1016/j.ijhydene.2022.08.056.

[49] S. Flesch, D. Pudlo, D. Albrecht, A. Jacob, and F. Enzmann, Hydrogen underground storage, Petrographic and petrophysical variations in reservoir sandstones from laboratory experiments under simulated reservoir conditions, Int. J. Hydrogen Energy 43(45) (2018) 20822–20835. https://doi.org/10.1016/j.ijhydene.2018.09.112.

[50] R.B. Bird, W.E. Stewart, E.N. Lightfoot, Transport Phenomena, 2nd ed., John Wiley & Sons, 2002.

[51] S. Roy, R. Raju, H.F. Chuang, B.A. Cruden, M. Meyyappan, Modeling gas flow through microchannels and nanopores, J. Appl. Phys. 93(8) (2003) 4870–4879. https://doi.org/10.1063/1.1559936.

[52] F. Javadpour, D. Fisher, M. Unsworth, Nanoscale gas flow in shale gas sediments, J. Can. Pet. Technol. 46(10) (2007) 55–61. https://doi.org/10.2118/07-10-06.

[53] E.A. Mason, A.P. Malinauskas, Gas Transport in Porous Media: The Dusty-Gas Model, Elsevier, 1983.

[54] R. Krishna and J. M. van Baten, Investigating the validity of the Bosanquet formula for estimation of diffusivities in mesopores, *Chemical Engineering Science* 69 (2012) 684–688. https://doi.org/10.1016/j.ces.2011.11.026.

[55] F. Civan, Effective correlation of apparent gas permeability in tight porous media, Transp. Porous Media 82 (2010) 375–384. https://doi.org/10.1007/s11242-009-9432-z.

[56] A. Ghanizadeh, S. Aquino, C.R. Clarkson, O. Haeri-Ardakani, H. Sanei, Petrophysical and Geomechanical Characteristics of Canadian Tight Oil and Liquid-Rich Gas Reservoirs, SPE-171633-MS, SPE/CSUR Unconventional Resources Conf.–Canada, Calgary, AB, Canada, 2014. https://doi.org/10.2118/171633-MS.

[57] E.A. Letham, R.M. Bustin, Klinkenberg gas slippage measurements as a means for shale pore structure characterization, Geofluids 16(2) (2016) 264–278. https://doi.org/10.1111/gfl.12147.

[58] B. Strauch, P. Pilz, J. Hierold, and M. Zimmer, Experimental simulations of hydrogen migration through potential storage rocks, *Int. J. Hydrogen Energy* 48 (2023) 25808–25820. https://doi.org/10.1016/j.ijhydene.2023.03.115.

[59] E. Jacops, K. Wouters, G. Volckaert, H. Moors, N. Maes, C. Bruggeman, R. Swennen, R. Littke, Measuring the effective diffusion coefficient of dissolved hydrogen in saturated Boom Clay, Appl. Geochem. 61 (2015) 175–184. https://doi.org/10.1016/j.apgeochem.2015.05.022.

[60] E. Salina Borello, S. Bocchini, A. Chiodoni, C. Coti, M. Fontana, F. Panini, C. Peter, C.F. Pirri, M. Tawil, A. Mantegazzi, F. Marzano, V. Pozzovivo, F. Verga, D. Viberti, Underground hydrogen storage safety: Experimental study of hydrogen diffusion through caprocks, Energies 17 (2) (2024) 394. https://doi.org/10.3390/en17020394.

[61] Y. Yang, C.W. Neil, E.J. Guiltinan, S. Mao, M. Mehana, Q. Kang, S. Liu, T.C. Germann, M.R. Gross, Experimental characterization of hydrogen diffusion in shale rocks for geologic storage applications, ACS Earth and Space Chemistry 9 (7) (2025) 1858–1870. https://doi.org/10.1021/acsearthspacechem.5c00092.

[62] J. Michelsen, B. Hagemann, L. Ganzer, W. Hujer, Measurement of hydrogen diffusion through caprock samples, in: Proceedings of the Sixth International Conference on Fault and Top Seals, Vienna, Austria, 26–28 September 2022, European Association of Geoscientists & Engineers, 2022, pp. 1–5. https://doi.org/10.3997/2214-4609.202243061.

[63] M. Ghaedi, P.Ø. Andersen, R. Gholami, Hydrogen diffusion into caprock: A semi-analytical solution and a hydrogen loss criterion, Journal of Energy Storage 64 (2023) 107134. https://doi.org/10.1016/j.est.2023.107134.

[64] A. Amann-Hildenbrand, B.M. Krooss, J. Harrington, R. Cuss, C. Davy, F. Skoczylas, E. Jacops, and N. Maes, Gas transfer through clay barriers, in: *Natural and Engineered Clay Barriers*, Developments in Clay Science, Vol. 6, Elsevier, 2015, pp. 227–267. https://doi.org/10.1016/B978-0-08-100027-4.00007-3.

[65] W.T. Pfeiffer, S. Bauer, Subsurface porous media hydrogen storage, scenario development and simulation, Energy Procedia 76 (2015) 565–572. https://doi.org/10.1016/j.egypro.2015.07.872.

[66] V. Vilarrasa, S. Olivella, J. Carrera, and J. Rutqvist, Long term impacts of cold CO_2 injection on the caprock integrity, *Int. J. Greenhouse Gas Control* 24 (2014) 1–13. https://doi.org/10.1016/j.ijggc.2014.02.016.

[67] T. B. Boving and P. Grathwohl, Tracer diffusion coefficients in sedimentary rocks: correlation to porosity and hydraulic conductivity, *Journal of Contaminant Hydrology* 53(1–2) (2001) 85–100. https://doi.org/10.1016/S0169-7722(01)00138-3.

[68] S. Hamamoto, P. Møldrup, K. Kawamoto, and T. Komatsu, Excluded-volume expansion of Archie's law for gas and solute diffusivities and electrical and thermal conductivities in variably saturated porous media, *Water Resources Research* 46 (2010) W06514. https://doi.org/10.1029/2009WR008424.

[69] N.R. Morrow, Physics and thermodynamics of capillary action in porous media, Ind. Eng. Chem. 62(6) (1970) 32–56. https://doi.org/10.1021/ie50726a006.

[70] G.R. Jerauld, S.J. Salter, The effect of pore-structure on hysteresis in relative permeability and capillary pressure: Pore-level modeling, Transp. Porous Media 5 (1990) 103–151. https://doi.org/10.1007/BF00144600.

[71] N.S. Muhammed, M.B. Haq, D.A. Al Shehri, A. Al-Ahmed, M.M. Rahman, E. Zaman, and S. Iglauer, Hydrogen storage in depleted gas reservoirs: A comprehensive review, *Fuel* 337 (2023) 127032. https://doi.org/10.1016/j.fuel.2022.127032.

[72] M. Hosseini, J. Fahimpour, M. Ali, A. Keshavarz, S. Iglauer, H_2–brine interfacial tension as a function of salinity, temperature, and pressure; implications for hydrogen geo-storage, J. Pet. Sci. Eng. 213 (2022) 110441. doi.10.1016/j.petrol.2022.110441.

[73] Y.T.F. Chow, G.C. Maitland, and J.P.M. Trusler, Interfacial tensions of (H_2O + H_2) and (H_2O + CO_2 + H_2) systems at temperatures of (298–448) K and pressures up to 45 MPa, *Fluid Phase Equilib.* 475 (2018) 37–44. https://doi.org/10.1016/j.fluid.2018.07.022.

[74] M. Xie, M. Zhang, Z. Jin, Machine learning-based interfacial tension equations for (H_2 + CO_2)-water/brine systems over a wide range of temperature and pressure, Langmuir 40 (10) (2024) 5369–5377. https://doi.org/10.1021/acs.langmuir.3c03831.

[75] M. Behnamnia, N. Mozafari, A. Dehghan Monfared, Rigorous hybrid machine learning approaches for interfacial tension modeling in brine-hydrogen/cushion gas systems: Implication for hydrogen geo-storage in the presence of cushion gas, J. Energy Storage 73 (2023) 108995. https://doi.org/10.1016/j.est.2023.108995.

[76] A. Al-Yaseri, L. Esteban, A. Giwelli, J. Sarout, M. Lebedev, and M. Sarmadivaleh, Initial and residual trapping of hydrogen and nitrogen in Fontainebleau sandstone using nuclear magnetic resonance core flooding, *Int. J. Hydrogen Energy* 47 (2022) 22482–22494. https://doi.org/10.1016/j.ijhydene.2022.05.059.

[77] E.M. Thaysen, I.B. Butler, A. Hassanpouryouzband, D. Freitas, F. Alvarez-Borges, S. Krevor, N. Heinemann, R. Atwood, and K. Edlmann, Pore-scale imaging of hydrogen displacement and trapping in porous media, *Int. J. Hydrogen Energy* 48 (2023) 3091–3106. https://doi.org/10.1016/j.ijhydene.2022.10.153.

[78] S. Iglauer, M. Ali, A. Keshavarz, Hydrogen wettability of sandstone reservoirs: Implications for hydrogen geo-storage, Geophys. Res. Lett. 48 (2021) e2020GL090814. https://doi.org/10.1029/2020GL090814.